



**Intelligent control mechanisms for enhanced
fault ride-through performance and provision of
ancillary services**



HydroFlex

Increasing the value of hydropower through increased flexibility

Deliverable 4.2 Intelligent control mechanisms for enhanced fault ride-through performance and provision of ancillary services

Work package	WP4 Flexibility of Generator and Converter
Task	Task 4.1 Grid interface and grid code adherence and support
Lead beneficiary	University of Strathclyde
Authors	Max Parker, Cagatay Cebeci, Luis Recalde-Camacho, David Campos-Gaona, Olimpo Anaya-Lara
Due date of deliverable	31.03.2022
Actual Submission date	31.03.2022
Type of deliverable	Report
Dissemination level	Public



This project has received funding from the European Union's Horizon 2020 research and innovation programme under grant agreement No 764011.

Executive Summary

This report presents the results of work carried out to develop a controller for a variable-speed hydropower plant, which is designed to enable provision of fast frequency support services during generating operation. The controller is designed around a hydropower plant consisting of a Francis turbine driving a synchronous generator, connected to the electrical grid through a fully-rated power converter, and is thus suitable for retrofitting to an existing installation.

The hydropower plant and electrical grid are modelled in Matlab/Simulink, using the Simscape electrical blockset. A waterway model consisting of headrace, surge tank and penstock is used, with a travelling-wave model used for the penstock to take account of water hammer effects. The turbine uses an Euler model for speed of computation, and is based around a high-head design. Built-in blocks are used for the generator and converter, with an averaged model used for the converter to reduce simulation time.

A controller has been developed in which a frequency-support controller determines the system power output based around a steady-state power demand modified by frequency droops, and taking account of the turbine speed to prevent undesired operating speeds. The modified power demand is sent to the grid-side converter, with the machine side converter, controlled using a vector current controller with field-oriented control, regulating the DC-link voltage. A governor based around a proportional-integral-derivative controller with power feedforward regulates the turbine speed. A Model Predictive Controller is also designed as a possible replacement of the proportional-integral-derivative controller to achieve a faster and smoother turbine speed regulation.

Finally, a virtual synchronous machine is implemented for the grid-side converter control, and is shown to be capable of emulating the generator inertia, as well as increased inertias, with improved damping characteristics.

Performance of the frequency support provision is verified in simulation using a stiff grid, and a representative electrical grid, with the variable-frequency operation resulting in a significantly reduced frequency dip during a loss of generation event.

Table of Contents

Executive Summary	2
Table of Contents	3
Abbreviations	4
1 Introduction	5
2 Model Design.....	6
2.1 Waterway and turbine	6
2.1.1 Waterway model	7
2.1.2 Turbine model	8
2.1.3 Example output	9
2.2 Electrical system	10
2.2.1 Generator model	10
2.2.2 Converter model.....	11
3 Controller Design.....	13
3.1 Turbine governor	14
3.2 Turbine governor – fixed speed	15
3.3 Model predictive control for turbine governor.....	17
3.4 Generator control	24
3.5 Grid-side control, virtual synchronous machine.....	27
3.5.1 Vector current controller	28
3.5.2 Virtual synchronous machine	30
3.5.3 Controller integration.....	31
3.5.4 Grid-side controller parameters.....	35
3.6 DC-link voltage controller.....	35
3.7 Frequency support controller	36
3.7.1 Operating limits.....	37
3.7.2 Controller structure.....	37
3.7.3 Example controller operation.....	39
3.7.4 Frequency support controller parameters	40
4 Simulated Performance.....	43
4.1 Stiff grid.....	43
4.1.1 Synthetic Inertia	43
4.1.2 Frequency Support.....	43

4.1.3	Over-frequency Response	46
4.1.4	Grid Fault Response	47
4.2	With grid model.....	49
5	Conclusion.....	55
6	References.....	56

Abbreviations

AC	Alternating Current
DC	Direct Current
DFIG	Doubly-Fed Induction Generator
EMF	ElectroMotive Force
MPC	Model-Predictive Control
PI	Proportional-Integral
PID	Proportional-Integral-Derivative
PLL	PhaseLock Loop
VCC	Vector Current Controller
VSHP	Variable-Speed HydroPower
VSM	Virtual Synchronous Machine

1 Introduction

There are many possible benefits to using variable-speed operation in hydroelectric power generation, through the use of a frequency converter between the generator and grid. The first installations were aimed at enabling variable power during the pumping operation of pumped-storage plants (Kuwabara, Shibuya, Furuta, Kita, & Mitsuhashi, 1996). This also has a benefit in the generating mode, as the ideal speeds for generating and pumping are different, and a compromise fixed speed can lead to a loss of efficiency or undesirable mechanical loads.

Various additional benefits can be realised (Mercier, Olivier, & Dejaeger, 2016) (Fraile-Ardanuy, Román Wilhelmi, Fraile-Mora, & Pérez, 2006) (Iliev, Trivedi, & Dahlhaug, 2019) (Nobile, Sari, & Schwery, 2018):

- Increased operating range in generating mode, as the turbine can be run at a lower speed for lower power outputs, reducing issues with vortex rope formation in the outlet.
- Better tracking of the maximum efficiency point over the power range.
- Improved dynamic performance, by decoupling the turbine speed from the grid frequency, allowing energy to be taken from the turbine inertia to provide instant power, not limited by the slower waterway dynamics.

The improvement in dynamic performance is particularly of interest in an electrical grid featuring a greater share of intermittent inverter-connected generation such as wind and solar power. This leads to a greater need to rapidly compensate for the variable output of these sources, made more difficult by the associated reduction in the amount of fast-reacting thermal generation, and the reduction in system inertia.

Some studies have investigated the use of variable-speed hydropower to directly compensate for the variation in output of a wind farm (Yang & Yang, 2019). This study is more concerned with the provision of frequency support services, which can represent a significant additional revenue stream to plant operators (Vargas-Serrano, Hamann, Hedtke, Franck, & Hug, 2017). The main emphasis is on the control system itself, and its performance in a small-scale representative grid, with the grid model being described in the previous Deliverable Report 4.1.

This Report will first describe the models used for the turbine, waterway, generator and converter. It will then describe the controllers, showing first the overall structure then the details of the design of individual control blocks. Finally, results will be given for simulations in a variety of scenarios based around a stiff grid and the representative grid.

2 Model Design

The model can be broadly divided into two parts: the hydraulic part consisting of the waterway and turbine, and the electrical part consisting of the generator and converter. There is also a grid model, which is covered in Deliverable Report 4.1.

2.1 Waterway and turbine

The configuration and parameters for the waterway and turbine models are taken from existing literature (Reigstad & Uhlen, 2020), and consist of a single Francis turbine with a short penstock and underground surge chamber, connected to the reservoir through a long headrace. The tailrace is considered to be short and have no effects on the dynamics, and the system has a relatively large head. The arrangement for the turbine and waterway is shown in Figure 1.

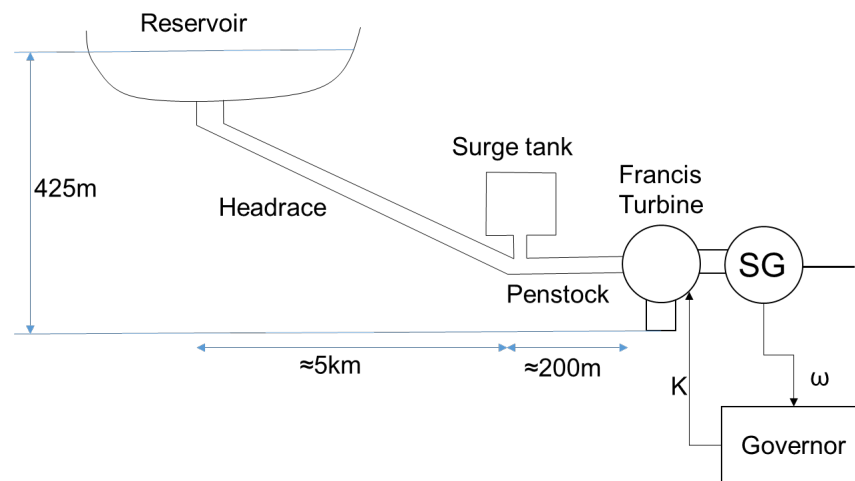


Figure 1 Turbine and waterway arrangement

The structure of the model is shown in Figure 2, and the waterway model is based on the widely-used methodology (Working Group on Prime Mover and Energy Supply Models for System Dynamic Performance Studies, 1992), with an inelastic flow model for the headrace and travelling wave-based elastic model for the penstock. The model works in the per-unit system, and the rated turbine power is 600MW.

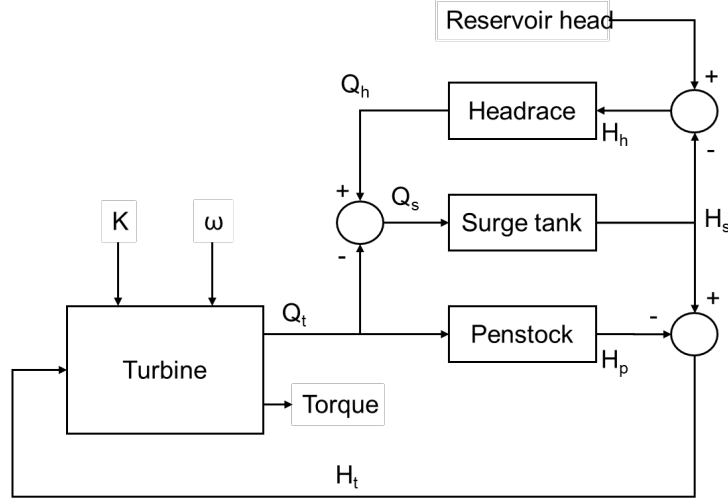


Figure 2 Turbine and waterway structure

2.1.1 Waterway model

The headrace flow, Q_h , is calculated using the non-elastic flow equation (1), where H_h is the headrace head, T_{Wh} is the water time constant for the headrace, f_{ph} is the friction factor for the headrace and s is the Laplace operator. The surge tank head, H_s , is calculated using (2), where Q_s is the flow into the surge tank, C_s is the surge tank storage constant, and f_o is the orifice loss.

$Q_h = \frac{H_h - f_{ph}Q_h Q_h }{T_{Wh}s}$	(1)
$H_s = \frac{Q_s}{C_s s} - f_o Q_s Q_s $	(2)

The penstock head, H_p , is calculated using a travelling wave equation shown in (3), where Q_p is the penstock flow, Z_0 the surge impedance, T_e the wave travel time and f_{pp} the friction factor for the penstock. The waterway model was initially implemented in Simulink as a continuous model, but when combined with the electrical model it was found to lead to a slow run time, due to the short time steps required by the converter. Because of this, the waterway model was discretised, with the discrete model for the penstock shown in (4).

$H_p = \frac{-Z_0(1 - e^{-2T_e s})}{1 + e^{-2T_e s}} Q_p - f_{pp} Q_p Q_p $	(3)
$H_p = \frac{-Z_0(1 - z^{-d})}{(1 + z^{-d})} Q_p - f_{pp} Q_p Q_p $	(4)

Here, z^{-d} represents a delay of d time steps, and $d = 2T_e f_s$, where f_s is the sampling frequency. The integrator in the headrace model was discretised using the backward Euler representation to avoid forming an algebraic loop and leading to slow simulation times. The integrator in the surge tank model was discretised using forward Euler as the orifice loss term already led to direct feedthrough, but a single sample delay was inserted to the output of the block to eliminate algebraic loops.

A time step of 1ms was used. The relatively short penstock has a wave travel time of 126ms, so this is fast enough relative to the model dynamics that discretisation effects are not noticed, and further tuning is not required. A longer timestep could be used, but would have little benefit as the waterway model now no longer has a significant impact on the simulation time. This could change if the model were used with a phasor-based model using a longer time step, rather than the EMT model used in this study, in which case further optimisation could be beneficial.

2.1.2 Turbine model

Several methods exist to model the turbine, which is represented as a variable throttle in Figure 2, giving a flow output for a given head, speed ω , and guide vane opening K , as well as the turbine torque. The method used in power systems studies (Working Group on Prime Mover and Energy Supply Models for System Dynamic Performance Studies, 1992) is simple to implement, but is based around a fixed speed system, so only allows small deviations around a fixed operating speed. On the other hand, a method based around lookup tables for the turbine characteristics, the Hills diagram, has a high accuracy across the operating range, but is difficult to implement as each input to the table does not necessarily have a unique output (Pannatier, et al., 2010). The Hills diagram must be found from scale model testing or high fidelity simulation.

A good compromise is to use a model based on the Euler equation, which relates to how the hydraulic power is changed to mechanical power in the shaft through changes of the water velocity vectors within the turbine (Nielsen, 2015) (Reigstad & Uhlen, 2020). This method cannot accurately represent the operating regions where unsteady flow occurs, but these would be avoided during normal operation in order to prevent damage to the turbine. This is only an issue during start-up when the turbine will transition through these regions.

The turbine flow, Q_t , is calculated as shown in (5), where K is the guide vane opening, ω the turbine speed, H_t the turbine head and σ is a constant. K_q is a gain factor relating to the fact that the rated flows for the turbine and waterway model are different.

$Q_t = K_q K \sqrt{H_t - \sigma(1 - \omega^2)}$	(5)
---	-----

The turbine mechanical torque T_t is given by (6), where m_s is the dimensionless starting torque, and ψ is a constant. The starting torque is given by (7), where ξ is a constant, α_1 is the guidevane angle and α_{1R} the guidevane angle for rated power. The relationship between α_1 and K is given by (8).

$T_t = \frac{Q_t}{H_t} (m_s - \psi\omega)$	(6)
--	-----

$m_s = \xi \frac{Q_t}{K} (\cos \alpha_1 + \tan \alpha_{1R} \sin \alpha_1)$	(7)
--	-----

$\sin \alpha_1 = K \sin \alpha_{1R}$	(8)
--------------------------------------	-----

The turbine model itself contains no dynamics, with the inertia included as part of the generator system, although a first-order low-pass filter with time constant 1s is applied to the guide vane demand, which represents the actuation servo response. Values for the waterway and turbine parameters are taken from (Reigstad & Uhlen, 2020), and are shown in Table 1.

Table 1 Waterway and turbine parameters

Waterway	Rated head	425	m
	Rated flow	170	m ³ /s
Headrace	f_{Ph}	0.02	s ⁴ /m ⁵
	T_{Wh}	4.34	s
Surge Tank	f_O	0.036	s ⁴ /m ⁵
	C_s	0.099	
Penstock	Z_0	9.61	
	T_e	0.126	s
	f_{Pp}	0.049	s ⁴ /m ⁵
Turbine	Rated head	425	m
	Rated flow	144	m ³ /s
	σ	0.015	
	ψ	0.404	
	ξ	0.918	
	α_{1R}	0.745	

2.1.3 Example output

An example of the hydroelectric system model output is shown in Figure 3, showing a guidevane demand step at 5s from 0 to 0.7. This is a somewhat extreme situation, with the guidevane opening rate normally restricted in the governor, but it serves to excite travelling-wave oscillations in the penstock, which are much less significant in amplitude compared with the other dynamics seen. It can be seen that the continuous and discrete models give virtually identical results.

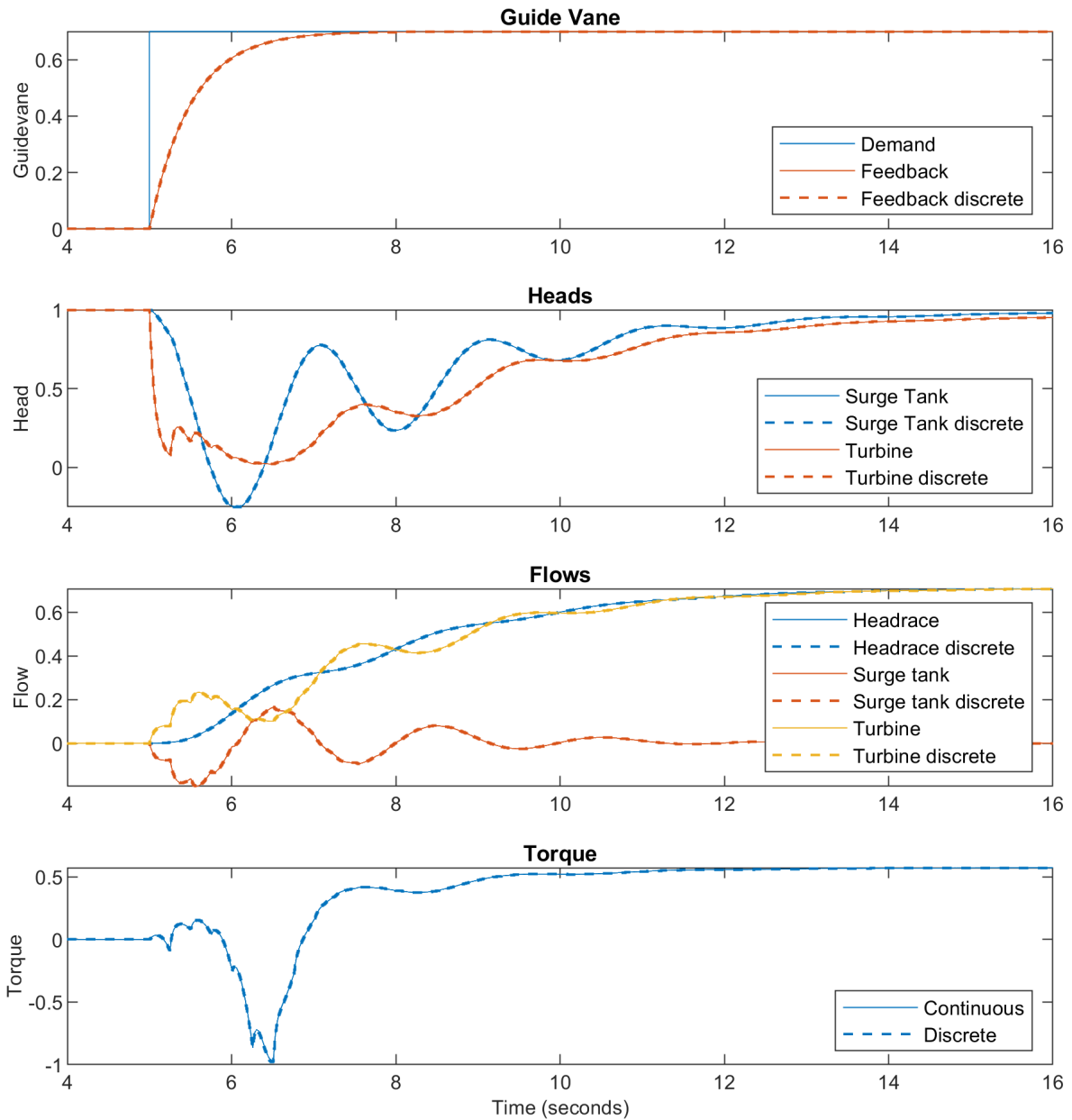


Figure 3 Example hydroelectric system simulation

2.2 Electrical system

The electrical part of the hydro system, and the network, are modelled in Simulink using the Specialized Power Systems blockset of Simscape. The structure of the electrical system is shown in Figure 4, and consists of a wound-field synchronous generator connected through a fully-rated back to back converter, and grid coupling inductance.

2.2.1 Generator model

The generator model implements a standard 5th order state space model, modelled in the d-q reference frame aligned to the rotor axis, and taking into account the dynamics of the field and damper windings. Parameters for the generator are typical for a large hydro generator (Krause, Wasynczuk, Sudhoff, & Pekarek, 2013), and are given in Table 2. The electrical system is modelled

in real-world units, but parameters for the generator (apart from the base quantities) are specified in per-unit.

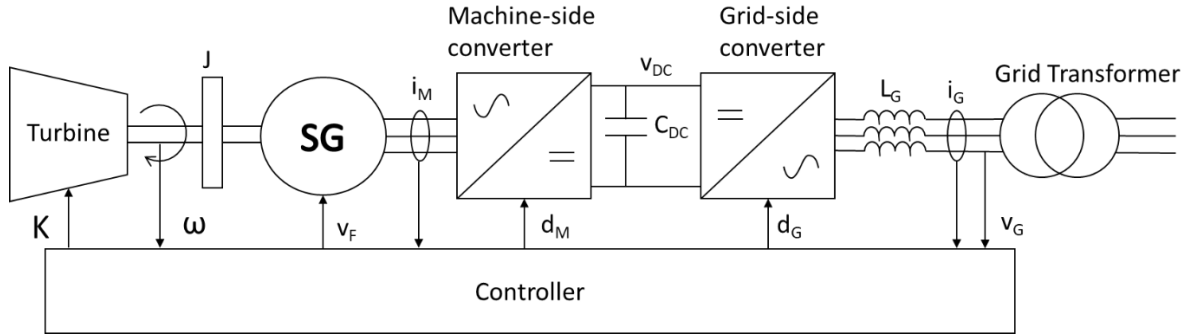


Figure 4 Electrical system arrangement

Table 2 Synchronous generator parameters

Rated Power		325	MVA
Line-line voltage		13.8	kV
Poles		64	
Rated frequency		50	Hz
Inertia constant		6.5	s
Stator resistance	r_s	0.0019	PU
Stator leakage reactance	X_{ls}	0.12	PU
Stator synchronous reactance, q-axis	X_q	0.48	PU
Stator synchronous reactance, d-axis	X_d	0.85	PU
Field resistance, referred to stator	r'_{fd}	0.00041	PU
Field leakage reactance, referred to stator	x'_{lfd}	0.249	PU
Damper resistance, q-axis, referred to stator	r'_{kq}	0.0136	PU
Damper leakage reactance, q-axis, referred to stator	X'_{lkq}	0.1029	PU
Damper resistance, d-axis, referred to stator	r'_{kd}	0.0141	PU
Damper leakage reactance, d-axis, referred to stator	X'_{lkd}	0.16	PU

2.2.2 Converter model

For the converter, an averaged model was used based on the universal bridge block, which represents the converter as voltage sources on the AC side and as a current source on the DC side, and for simplicity it does not represent any losses and switching device voltage drops. The use of an averaged model greatly reduces the simulation step size compared with a model representing the converter switching.

Existing variable-speed hydropower systems have been of either relatively low power rating, or making use of doubly-fed induction generators (DFIGs) with partially-rated converters. For the DFIG-based systems, early installations used thyristor-based cycloconverters (Kuwabara, Shibuya, Furuta, Kita, & Mitsuhashi, 1996), producing a low-frequency output, but more recent DFIG-based and fully-rated systems have used 2- and 3-level voltage-source converters (Valavi & Nysveen, 2016). These usually require transformers to match the lower converter voltage to the higher generator voltage, or to allow for multi-level operation.

For larger systems, of 100MW and above, it is expected that converters based on the modular multilevel converter (MMC) will be used, with ABB already producing designs for such a converter designed for this application (Steimer, Senturk, Aubert, & Linder, 2014). These converters are starting to be used in high voltage direct current (HVDC) power transmission, and allow for a higher AC voltage so that the converter can be interfaced to the generator without the use of a transformer, as well as a low-distortion AC waveform.

For the electrical model, it is assumed that an MMC will be used, but the converter is modelled as a simple averaged model as the adaptation of an MMC control system to VSHP operation is considered to be outside the scope of this deliverable. The main effect of using an MMC in this case is that a higher sampling frequency can be used, while this is limited by the lower switching frequency in a converter with a lower number of levels. In addition, a simple grid coupling inductance is used where a simpler converter type would need a more complex LCL filter, with implications for the converter control that would be outside the scope of the deliverable.

Parameters for the converter are shown in Table 3. In an MMC, the grid inductance and resistance would be fairly typical, and arise due to the arm inductance, with the resistance representing the losses in the converter. There will also be an inductance on the generator side, but this is difficult to model as the generator is represented as a current source in the model, meaning that inductors cannot directly be connected to the terminals. Instead, any coupling inductance could be added to the generator stator leakage inductance.

Table 3 Converter parameters

Rated power	325MW	
Rated AC voltage	13.8kV	
DC-link voltage	22kV	
Sampling frequency	5kHz	
DC-link capacitance	750 μ F	
Grid inductance	187 μ H	0.1PU
Grid resistance	0.59m Ω	0.001PU

Within the model, the converter parameters are set in per-unit, or scaled with converter power and voltage rating in the case of the DC-link capacitance, so the converter rating can easily be changed. As will be described later, the controller operates in the per-unit system, with measurement scaling occurring at the point the voltages and currents are measured, so it is also independent of converter voltage and current rating.

3 Controller Design

This report is primarily concerned with the provision of fast frequency support services using variable speed hydropower. Response speed in conventional hydropower is limited by the waterway dynamics, and variable speed operation gets around this limitation by allowing energy to be borrowed from the turbine inertia in the short term. This slows down the turbine, with the turbine speed being recovered as the water flow increases.

This is possible in generating mode as the power output of the turbine is decoupled from the turbine speed, within limits. In pumping mode for a pumped-storage system, the guide vanes are normally held fully open, with the pumping power determined by the turbine speed (Mercier, Olivier, & Dejaeger, 2016). While variable pumping power is a benefit of a variable-speed system, it does not allow for fast frequency response services as the power is coupled to the turbine speed. For this reason, this report will concentrate on generating operation.

Parameters that can be controlled are the electrical power, through the converter, and the hydraulic power, through the guide vanes. This leads to two possible methods (Kuwabara, Shibuya, Furuta, Kita, & Mitsuhashi, 1996): firstly the generator speed can be regulated using the electrical power, and the system power output set by the guide vanes. This allows control of the turbine speed to maximise efficiency and prevent waterway transients from reaching the grid. Secondly, the generator speed can be regulated using the turbine guide vanes, with the converter determining the grid power. This method is led by the grid requirements and is therefore more suited to the provision of frequency response services.

The overall control structure is shown in Figure 5. The machine- and grid-side controllers regulate the power transferred from the generator and to the grid respectively, with the DC-link voltage controller regulating the voltage of the DC link between the converters. This can be regulated using either converter, with the other determining the electrical power transfer, and the controller may need to switch between these two modes depending on circumstances. The turbine governor regulates the turbine speed through the guide vane position, and also takes a power demand as a feedforward. The frequency support controller determines the overall power demand based on a steady-state demand, modified with an additional demand related to the grid frequency through various frequency droop settings.

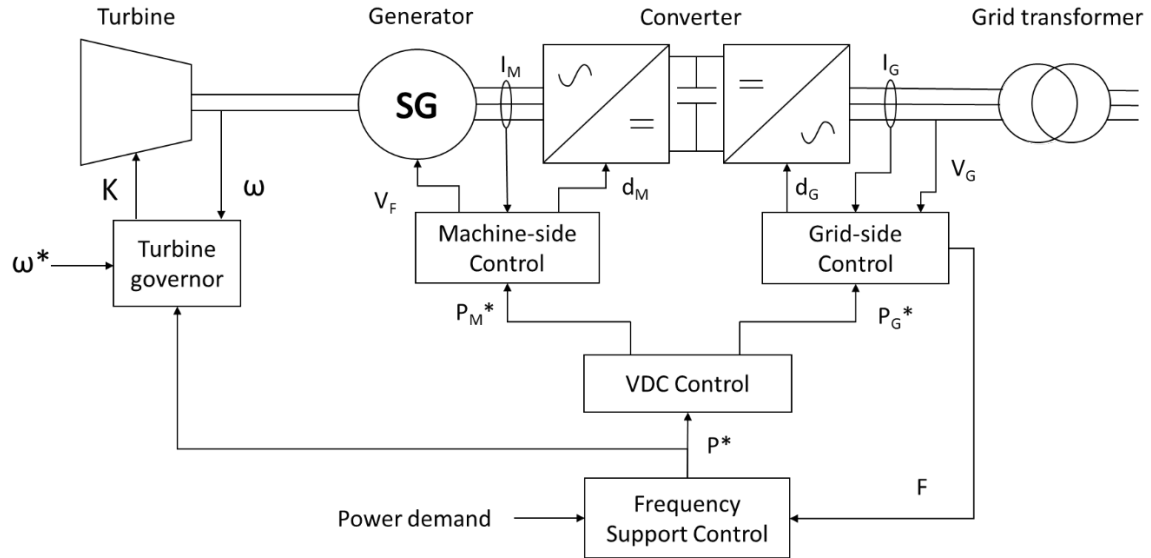


Figure 5 Overall control structure

A key additional function of the frequency support controller is to monitor the turbine operating condition, and to prevent the turbine entering any undesirable operating modes. This includes maximum and minimum speeds, as well as minimum power levels for a given speed. This will be discussed further in the section on the frequency support controller.

3.1 Turbine governor

The turbine governor regulates the turbine speed ω using the guide vane position demand K^* , and is based around a proportional-integral-derivative (PID) controller shown in Figure 6. The structure and parameters are largely taken from the same source as the turbine and waterway model parameters (Reigstad & Uhlen, 2020), but with the addition of anti-windup for the integrator via back-propagation, and feedforward of the power demand for improved performance.

The guide vane position demand is rate-limited, as is standard in hydropower, which minimises the negative-phase behaviour of the waterway and prevents pressure peaks in the pipes. In addition, the dynamics of the actuator servo will have an effect on the response, and these are included in the turbine model, so the governor uses a guidevane position feedback signal K_{FB} for the anti-windup control. Anti-windup uses the pre-limited controller output through a single-cycle delay $1/Z$, along with a gain K_W , to limit the integrator input.

The guidevane feedforward signal K_{FFD} is calculated using a lookup table based on the power demand and the generator speed. Governor parameters are given in Table 4.

Table 4 Turbine governor parameters

Proportional gain	K_P	3
Integral gain	K_I	0.1
Derivative gain	K_D	1
Anti-windup gain	K_W	1
Rate limit		$\pm 0.05\text{s}^{-1}$
Sampling frequency		100Hz

The response of the hydraulic system and turbine governor to an instantaneous step in electrical power of 0.1PU is shown in Figure 7 for several initial power outputs, with the turbine speed setpoint at 1PU. There is an initial sharp decrease in turbine speed, and the guidevanes start to open limited by the rate limiter. As the mechanical torque exceeds the electrical, the turbine speed starts to recover, and as this occurs the guidevane position is closed slightly towards the final value.

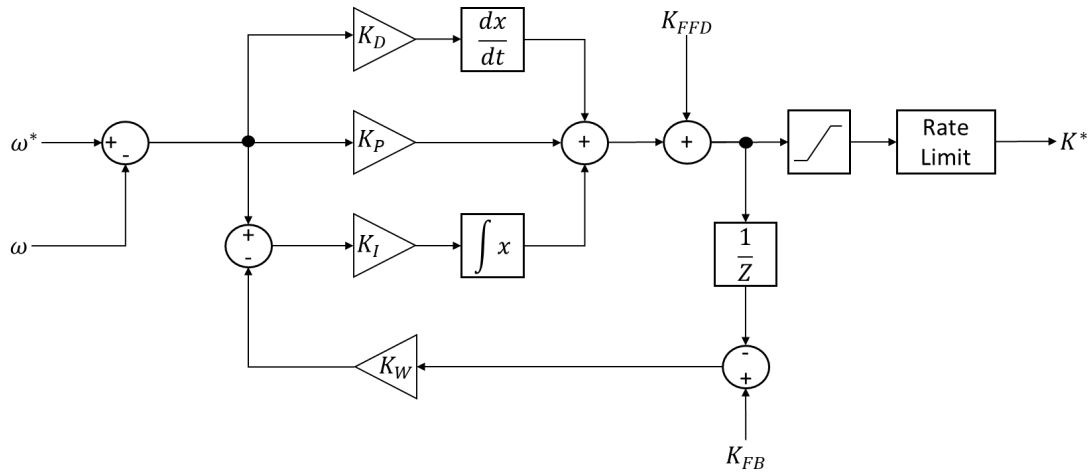


Figure 6 Turbine governor structure

3.2 Turbine governor – fixed speed

For comparison with a variable-speed system, a fixed-speed system was also implemented, using the same hydraulic model and generator. For the governor, a conventional proportional controller with transient droop was implemented (Working Group on Prime Mover and Energy Supply Models for System Dynamic Performance Studies, 1992), as shown in Figure 8.

Parameters for the governor are taken from the same source as for the variable-speed governor (Reigstad & Uhlen, 2020), and are given in Table 5.

Table 5 Fixed-speed governor parameters

Permanent droop	R_P	0.05
Transient droop	R_T	0.4
Governor time constant	τ_P	4s
Reset time	τ_R	5s
Rate limit		$\pm 0.05s^{-1}$

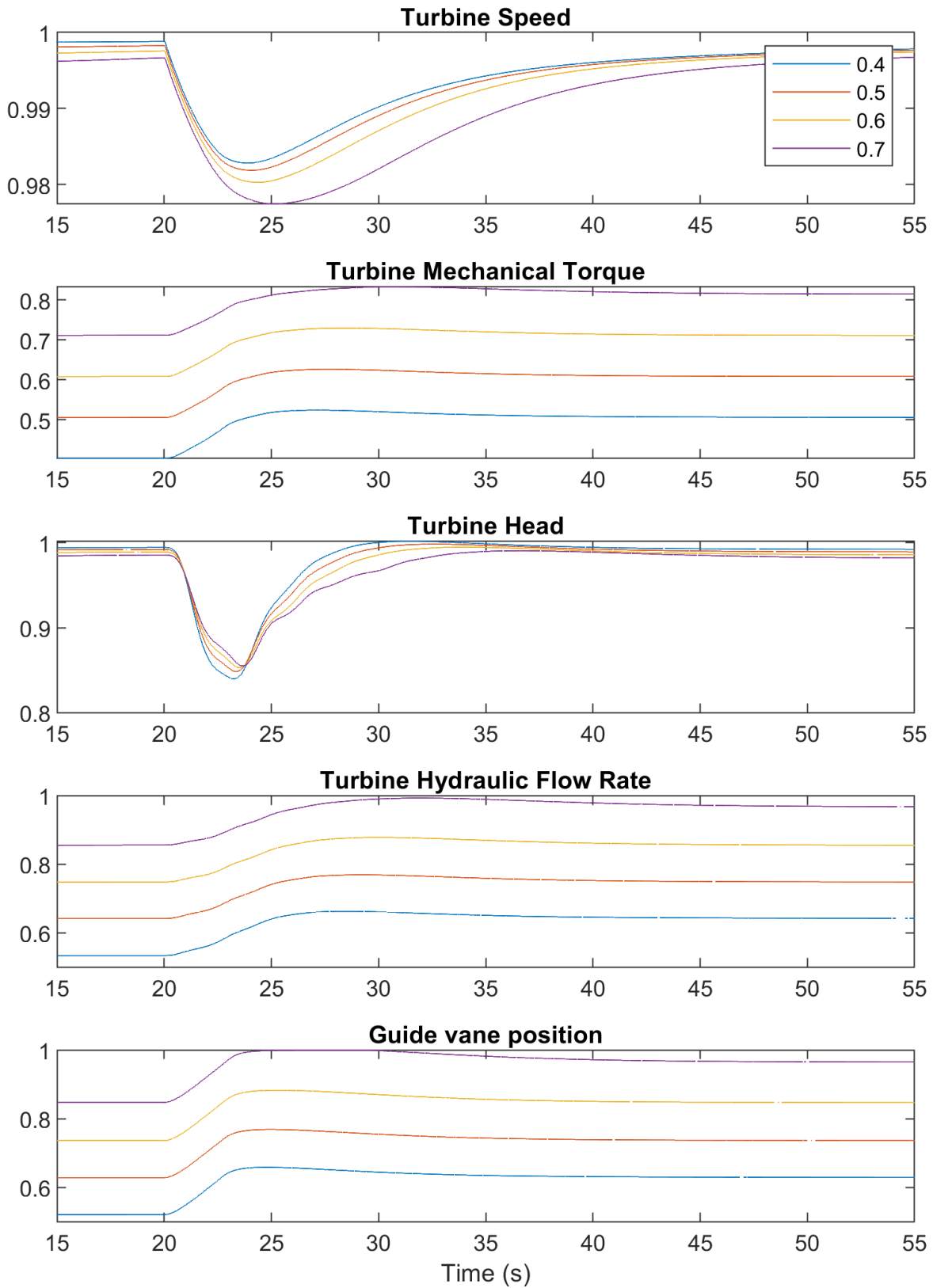


Figure 7 Governor response to 0.1PU increase in electrical power, for initial power of 0.4 to 0.7 PU

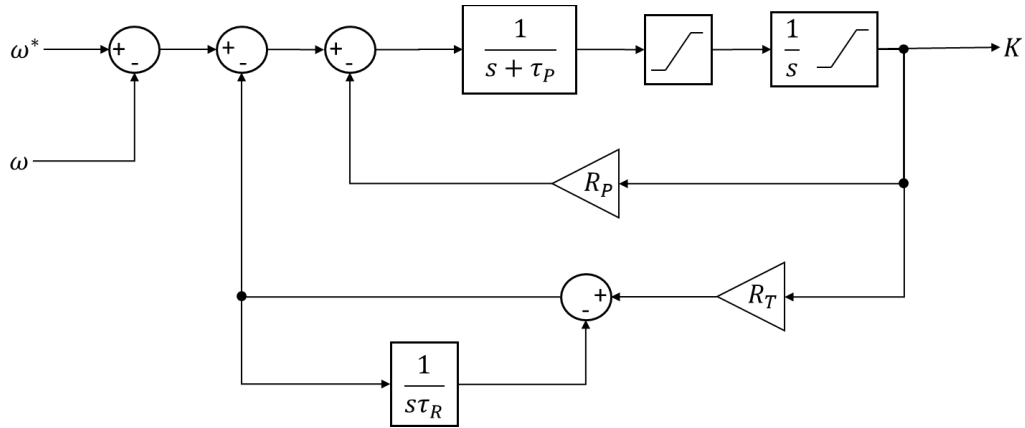


Figure 8 Fixed-speed governor

3.3 Model predictive control for turbine governor

For conventional fixed-speed hydropower plants, various controller improvements have been proposed, with model-predictive control (MPC) proving a promising option. MPC is a discrete closed-loop optimal controller in which a vector control signal is obtained by solving an optimisation problem over a prediction horizon from $t = t_0$ to $t = T_s H_p$, with sampling time $T_s = \frac{1}{f_s}$. Only the first sample of the vector control signal is used and the optimisation problem is recalculated at the next time step with the new initial state values (Reigstad, T.I., & Uhlen, K., 2020). MPC controllers, although more complex, offer faster and smoother response, lower rise time, settling time and overshoots, and they are more robust. However, the main performance improvements from MPC come from the ability to better handle the non-linear characteristics of the turbine and waterway (Zhang, Chen, & Ma, Nonlinear Predictive Control of a Hydropower System Model, 2015) (Beus & Pandžić, 2018) (Zhang, Chen, Yao, Ba, & Ma, 2017), provided a proper system model is available for the MPC design. Plants in which multiple turbines share the same waterway can benefit particularly (Muñoz-Hernández & Jones, 2006), as the control characteristics will change significantly depending on the number of turbines operating at the time. Further improvements in system stability can be gained by the combined control of the turbine guidevanes and generator excitation (Zheng, et al., 2016).

For variable-speed systems, linear MPC can be used to handle the internal control of the VSHP while a VSM can improve the power response to frequency deviations. In (Reigstad, T.I., & Uhlen, K., 2020) this coordinated control scheme is used with a Kalman filter to estimate unmeasured variables in the hydraulic system (headrace tunnel flow and penstock flow). In (Reigstad, T.I., & Uhlen, K., 2021) and (Reigstaf, T.I., & Uhlen, K., 2021) nonlinear MPC and moving horizon estimator have been used to improve the optimisation problem and achieve better performance. Nonlinear MPC has also been used locally for hydro turbine governor control only (Zhou, W., Thoresen, H.M., & Glemmstad, Bjorn, 2012), (Zhang, R., Chen, D., & Ma, X., 2015). Other nonlinear approximations of MPC, where the systems is reformulated to account for its nonlinear characteristics, are quasi Linear Parameter Varying (qLPV) state-space system (Briat, 2015) (Balas, 2002) and state-dependent systems (Cloutier, 1997).

3.3.1 MPC controller formulation

In this report, a local output feedback linear MPC is designed. At the governor, the MPC solves an optimisation problem to find the optimal turbine speed, while handling constraints defined in the model quadratic cost function. The optimisation problem is given by:

$$\min_{x \in \mathbb{R}^n, u \in \mathbb{R}^m} f(x, u) = \sum_{k=0}^{H_p-1} \frac{1}{2} x_{k+1}^T W_x x_{k+1} + \sum_{k=0}^{H_c} \frac{1}{2} u_k^T W_u u_k + \frac{1}{2} \epsilon^T W_\epsilon \epsilon \quad (9)$$

Subject to

$$\begin{aligned} x_{k+1} &= Ax_k + Bu_k + v_k & k = 0, \dots, H_p - 1 \\ x^{low} - \epsilon &\leq x_k \leq x^{high} + \epsilon \\ u^{low} &\leq u_k \leq u^{high} \end{aligned} \quad (10)$$

Where $x_k \in \mathbb{R}^n$ is the state vector, $u_k \in \mathbb{R}^m$ is the input vector, $v_k \in \mathbb{R}^l$ is the measured disturbance and ϵ is a nonnegative slack variable which quantifies the worst-case constraint violation. Variables x^{low} , u^{low} and x^{high} , u^{high} are state and input minimum and maximum limits. Variables H_p and H_c are the prediction and control horizons, respectively, that the cost function uses to solve the optimisation problem. Finally, W_x , W_u , W_ϵ are positive definite tuning weights.

3.3.2 MPC dynamic model

The state space model in (10) represents the linearised and discretised MPC dynamic model of the turbine, waterway structure, the mechanical system and the electrical system. Equations (1)-(8) represent the turbine and waterway model whereas the electrical system and the mechanical system are given by equations (11) and (12), respectively,

$$P_{base}/\omega = T_e \quad (11)$$

$$\omega = \frac{1}{2H} \int (T_t - T_e) dt \quad (12)$$

where H is a constant. Using (5)-(8), and assuming ($K_q = 1$), the mechanical torque is calculated as in (13).

$$T_t = \frac{Q_t}{H_t} \left(\xi \frac{Q_t}{K} (K \cos \alpha_{1R} + \tan \alpha_{1R} K \sin \alpha_{1R}) - \psi \omega \right) \quad (13)$$

Taking the derivative of the mechanical system in (12) leads to the following expression.

$$\dot{\omega} = \frac{1}{2H} (T_t - T_e) \quad (14)$$

Finally, substituting (11) and (13) into (14), the dynamics of the turbine speed, $\dot{\omega}$ are given by

$$\dot{\omega} = -\frac{1}{2H} \left(\frac{Q_t}{H_t} \psi + \frac{P_{base}}{\omega^2} \right) \omega + \frac{1}{2H} \left(\xi \frac{Q_t}{K} (\cos \alpha_{1R} + \tan \alpha_{1R} \sin \alpha_{1R}) \right) K \quad (15)$$

The highly nonlinear dynamics in (15) combined with the nonlinear dynamics of the turbine and waterway can be formulated in the following nonlinear state-space equations:

$$\begin{aligned}\dot{x} &= f(x, u, v) \\ y &= Cx\end{aligned}\quad (16)$$

where $x = [H_p \quad Q_h \quad H_s \quad \omega]^T$ is the state vector, $u = K$ is the system input, $v = P_{base}$ is the measured disturbance and $C = [0 \quad 0 \quad 0 \quad 1]$ is output parameters vector such that the system output, y , is turbine speed. The MPC dynamic model can be obtained by linearising (16) about equilibrium operating points $x_0 = [H_{p0} \quad Q_{h0} \quad H_{s0} \quad \omega_0]^T$, $u_0 = K_0$. The MPC linearised dynamic model is given by

$$\begin{aligned}\Delta\dot{x} &= A\Delta x + B\Delta u + v \\ y &= Cx\end{aligned}\quad (17)$$

where

$$A = \left. \frac{\partial f(x, u)}{\partial x} \right|_{(x_0, u_0)} = \begin{bmatrix} \frac{\partial f_1(x, u)}{\partial x_1} & \dots & \frac{\partial f_1(x, u)}{\partial x_4} \\ \vdots & \ddots & \vdots \\ \frac{\partial f_4(x, u)}{\partial x_1} & \dots & \frac{\partial f_4(x, u)}{\partial x_4} \end{bmatrix}_{(x_0, u_0)} ;$$

$$B = \left. \frac{\partial f(x, u)}{\partial u} \right|_{(x_0, u_0)} = \begin{bmatrix} \frac{\partial f_1(x, u)}{\partial u_1} & \frac{\partial f_1(x, u)}{\partial u_2} \\ \vdots & \vdots \\ \frac{\partial f_4(x, u)}{\partial u_1} & \frac{\partial f_4(x, u)}{\partial u_2} \end{bmatrix}_{(x_0, u_0)} ;$$

$\Delta x = x - x_0$, $\Delta u = u - u_0$ and v is assumed to be a disturbance and therefore not included during the linearisation.

The MPC dynamic model is discretized explicitly with sampling time $T_s = 0.1s$, that is

$$\begin{aligned}x_{k+1} &= A_d x_k + B_d u_k + v_k \\ y_k &= C x_k\end{aligned}\quad (18)$$

with $A_d = 1 + T_s A$ and $B_d = T_s B$ and the Δ term has been dropped for convenience as the MPC will be tested around the operating point.

Since the controller is an output-feedback MPC, a discrete Kalman filter is used to estimate the MPC discretised dynamic model states. The Kalman filter equations are

$$\begin{aligned}\hat{x}_{k+1|k} &= A_d \hat{x}_{k|k-1} + B_d u_k + v_k + L(y_k - \hat{y}_k) \\ \hat{y}_k &= C \hat{x}_{k|k-1}\end{aligned}\quad (19)$$

where y_k represents the measured system output, $\hat{x}_{k|k-1}$ and \hat{y}_k are the estimated states vector and estimated system output, respectively. The Kalman gain L is derived by solving a discrete Riccati equation. The resulting state-space equation is

$$\hat{x}_{k+1|k} = (A_d - LC) \hat{x}_{k|k-1} + [B_d \quad L] \begin{bmatrix} u_k \\ y_{m,k} \end{bmatrix} + v_k\quad (20)$$

$$\hat{y}_k = C\hat{x}_{k|k-1}$$

The closed-loop system representation of the complete VSHP plant with a MPC controller is illustrated in Figure 9, where turbine speed ω^* is the reference signal and ω is the output signal. The MPC control also uses the variable P_{base} (demanded electrical power) as its measured disturbance signal.

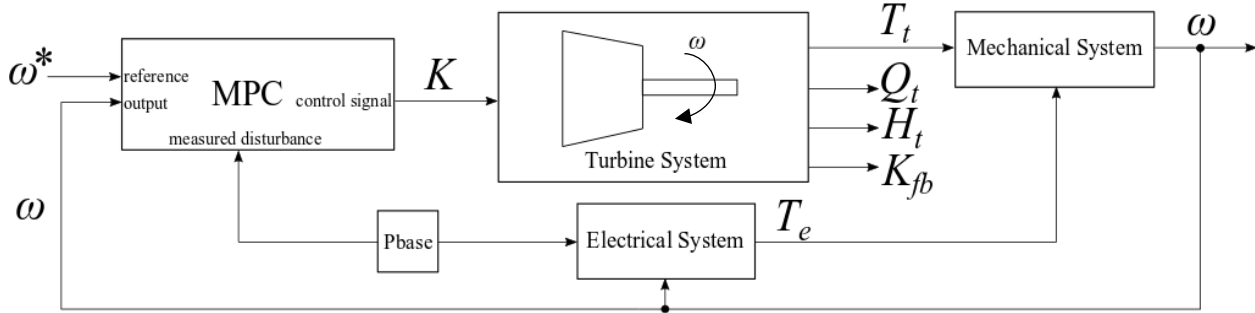


Figure 9 MPC control diagram

3.3.3 MPC controller settings and simulation results

The MPC control solution is obtained by the minimization of (9) over the prediction horizon $H_p = 30$, and the control horizon $H_c = 5$, using the quadratic programming approach adopted by Mathworks' Model Predictive Control toolbox. The error weighting $W_e \cong 0.644$ is to penalize deviation from the target value ω^* and the control rate weighting $W_{\Delta K} \cong 0.155$ is to penalize aggressive control. The controller output and its rate of change are constrained by $0 \leq K \leq 1$ and $-0.1 \leq \Delta K \leq 0.1$.

The responses of the inelastic hydraulic system and the MPC turbine governor are shown in Figure 10 where the control objective is the tracking of the reference turbine speed at $\omega^* = 1PU$. The demanded electrical power is initialized as $P_{base} = 0.7PU$ where an instantaneous step with the magnitude of $0.1PU$ is applied at $t = 40s$. The MPC control signal has a fast response and stays within the constraints. As a result, turbine speed reaches the steady-state value rapidly at both the start of the operation and the step change without displaying any significant undershoots or overshoots in the output signal. The hydraulic system elements such as surge tank head H_s , turbine head H_t , the headrace flow Q_h , surge flow Q_s are also demonstrated and the results show that they reach their steady-state values.

In Figure 11, The MPC governor response case has been extended by considering several different instantaneous steps initialized as $0.4PU$ to $0.7PU$, and, comparisons with the PID governor of section 3.1 have been made. The results show that the MPC is much faster than the PID with smaller rise time and settling time. The MPC also behaves more robustly under disturbances, demonstrating much smaller undershoots and zero or insignificant overshoots.

The MPC performance, in addition to the weightings provided above, can be further tuned by modifying manipulated variable rate weight on the controller and the output variable weight. For the results in Figure 10 and 11, the latter is decreased for tighter reference tracking and the maximum elimination of overshoots. The output variable weight can also be increased to provide

smoother control action as shown in Figure 12. However, this leads to overshooting in some cases therefore the weights have been tuned more aggressively.

To verify the graphical results, the root-mean-squared error (RMSE) of the MPC and PID responses under the impact of different instantaneous steps are also given in Table 6.

Table 6 RMSE results for MPC and PID

	0.7 PU	0.6 PU	0.5 PU	0.4 PU
$RMSE_{MPC}$	0.0034	$4.0235e - 04$	$8.5980e - 05$	$5.6968e - 05$
$RMSE_{PID}$	0.0107	0.0048	0.0034	0.0098

The results show that the RMSE values of MPC are smaller than those of the PID.

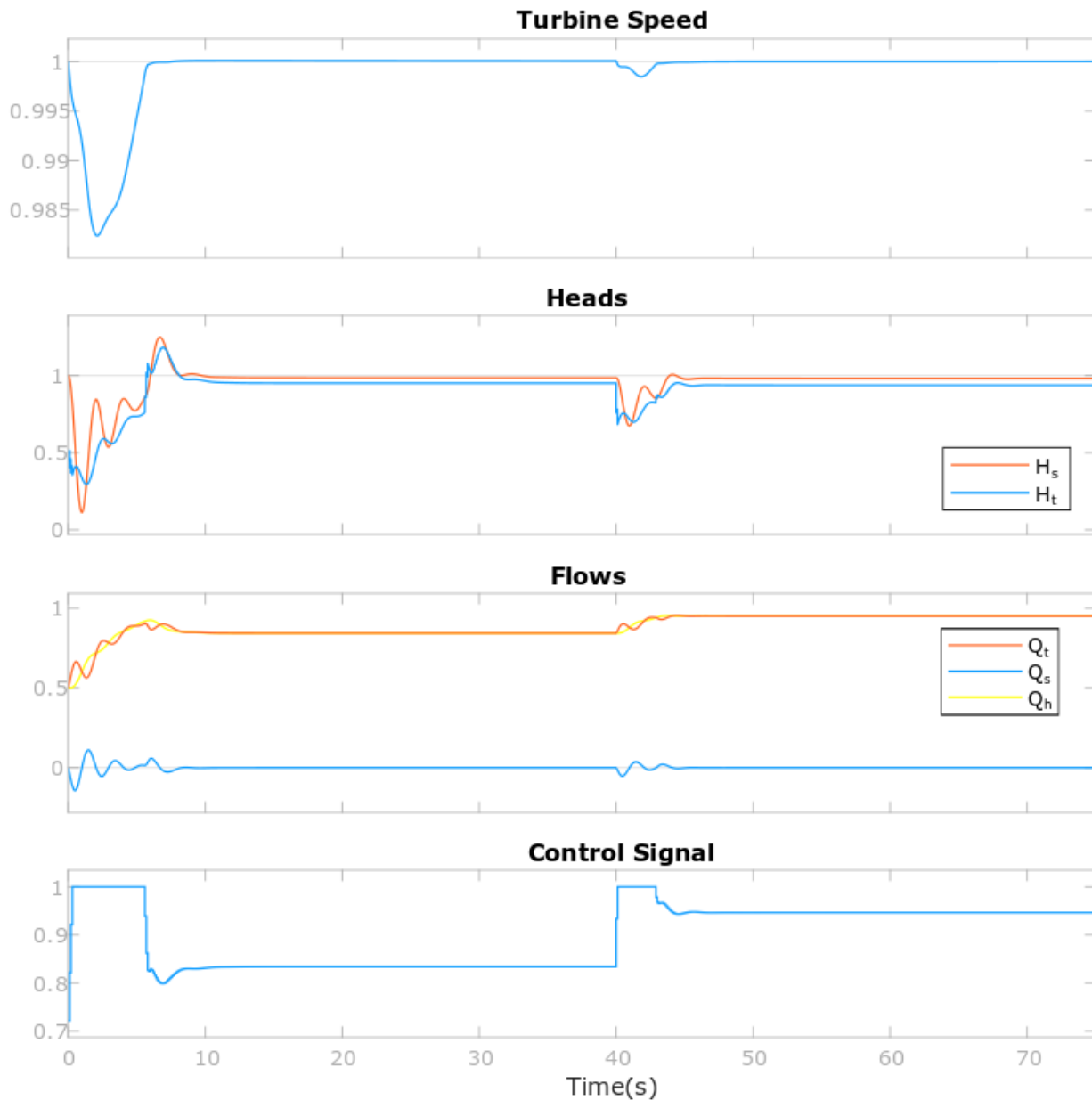


Figure 10 MPC governor response to 0.1PU increase in electrical power, for initial power of 0.7 PU

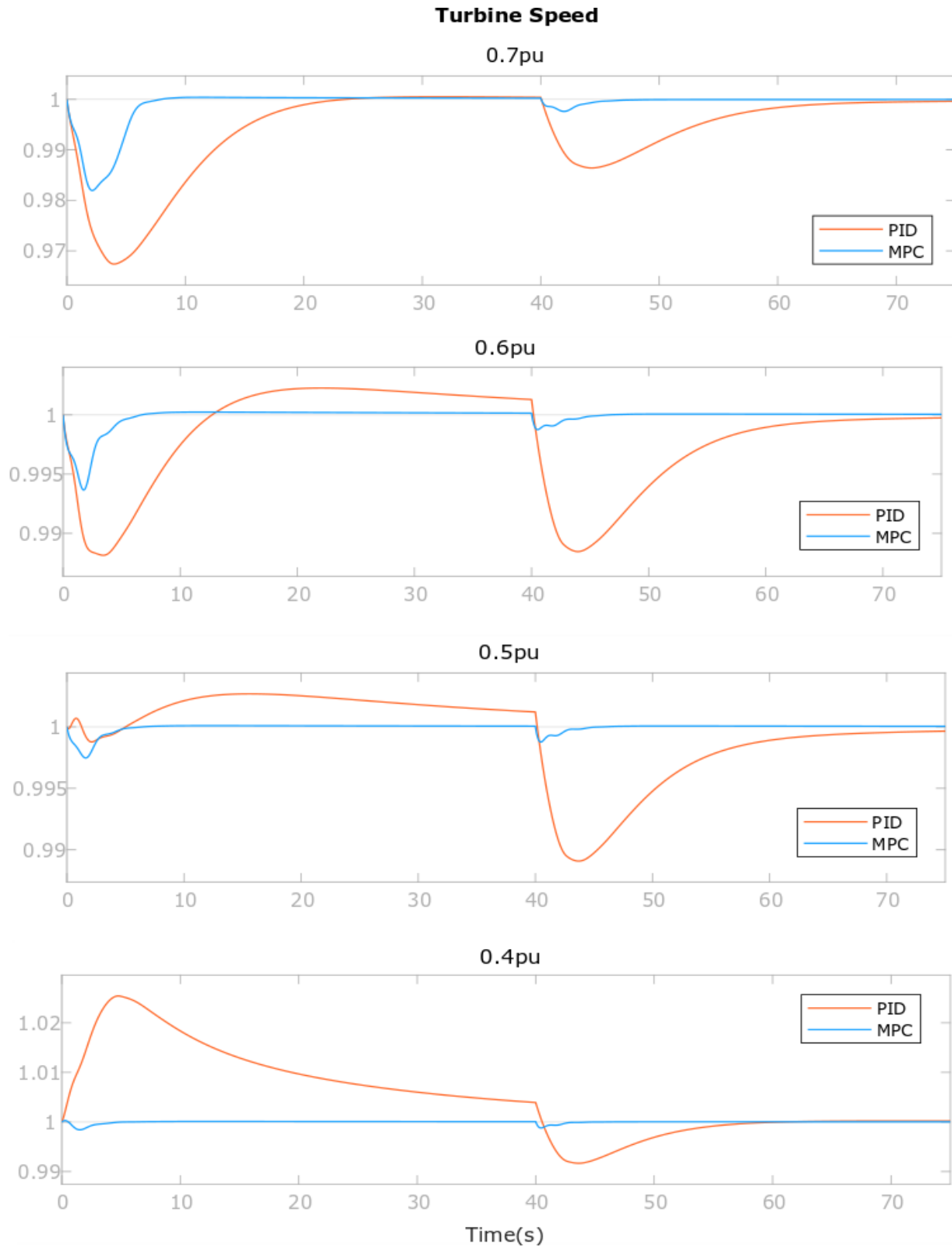


Figure 11 MPC and PID Governor responses to 0.1PU increase in electrical power, for initial power of 0.4 to 0.7 PU (aggressive tuning)

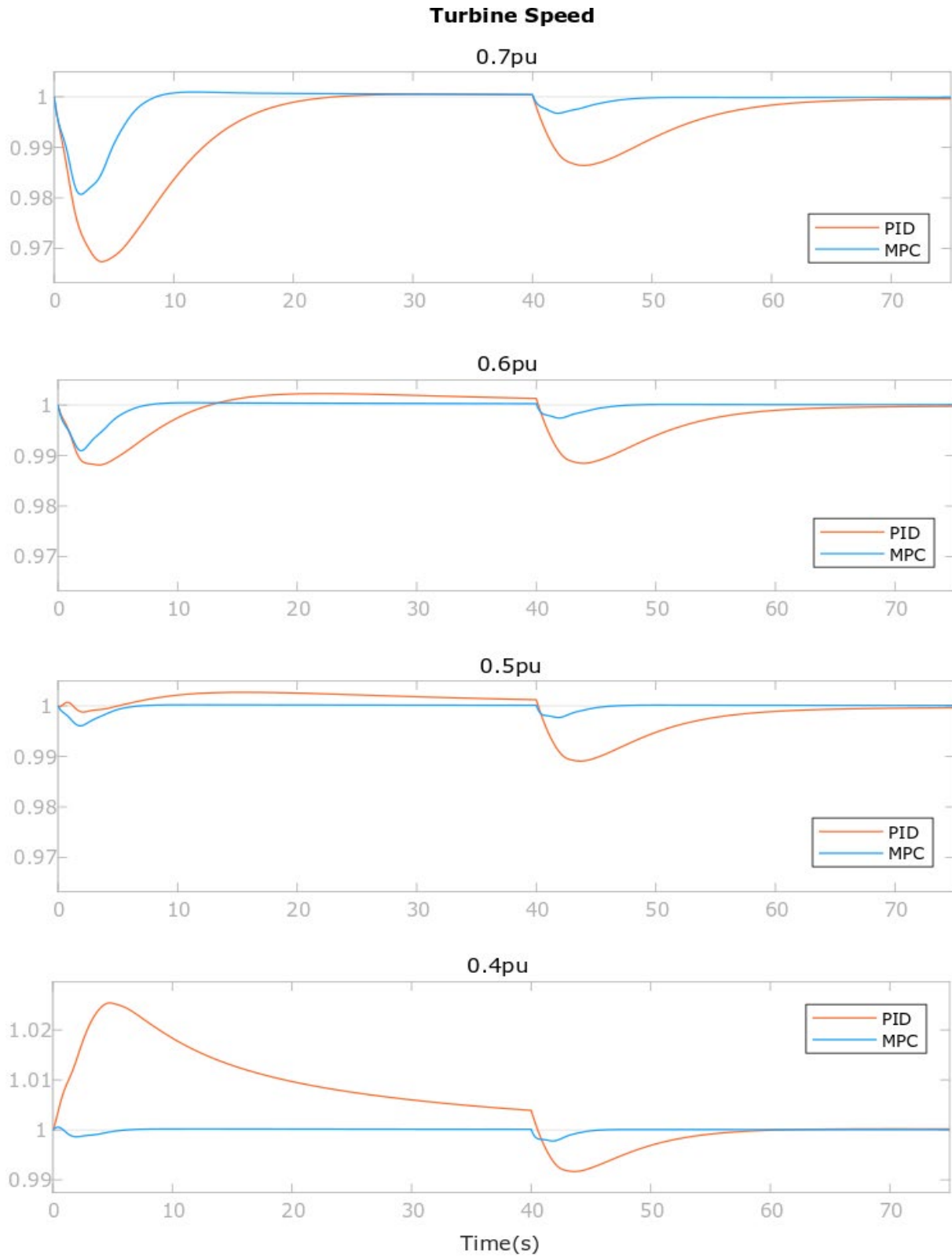


Figure 12 MPC and PID Governor responses to 0.1PU increase in electrical power, for initial power of 0.4 to 0.7 PU (smoother tuning)

3.4 Generator control

The generator-side converter controller uses field-oriented control to regulate the generator electrical torque, through controlling the stator current in the rotor reference frame, as well as the field current. In the per-unit system used in the controller, the electrical torque is given by (21), where $\phi_{d,qs}$ is the stator flux linkage and $i_{d,qs}$ is the stator current. Given knowledge of the stator flux linkage, the current demands $i_{d,qs}^*$ can be calculated and used in a current controller.

$T_e = \phi_{ds}i_{qs} - \phi_{qs}i_{ds}$	(21)
---	------

Stator flux can be estimated by an observer system, based on the stator and field currents, machine speed and applied voltages (Ogasawara, Akagi, & Nabae, 1988) (Uzel, Zeman, Peroutka, & Danek, 2012). However, this is not trivial as the damper winding currents are unknown and have to be estimated. As flux estimation is a known process, and tangential to the main aims of the project, it was decided to simplify the control system by using the values of the mutual flux provided by the generator model. This is analogous to the values provided by flux sensors placed in the generator airgap, which is a viable solution for a generator of this size. The stator flux linkages are given by (22) and (23), where L_{ls} is the stator leakage inductance and $\phi_{md,q}$ is the mutual flux linkage.

$\phi_{ds} = L_{ls}i_{ds} + \phi_{md}$	(22)
$\phi_{qs} = L_{ls}i_{qs} + \phi_{mq}$	(23)

The stator current is controlled using a conventional vector current controller. The voltage equation for the stator is given by (24) and (25) based on the stator flux, where ω_r is the rotor angular frequency, and R_s the stator winding resistance. If the damper and field windings are ignored, as in a permanent-magnet generator, then $\phi_{d,qs} = L_{d,q}i_{d,qs}$, and (24) and (25) are transformed into a familiar form.

$V_d = i_{ds}R_s - \omega_r\phi_{qs} + \frac{d\phi_{ds}}{dt}$	(24)
$V_q = i_{qs}R_s + \omega_r\phi_{ds} + \frac{d\phi_{qs}}{dt}$	(25)

This leads to the controller structure shown in Figure 13, which incorporates cross-coupling terms and feedforward of the generator EMF. Initial tuning of the controllers was carried out using the internal model method (Harnefors & Nee, 1998), for a PI controller with structure given by (26). The controller gains are given by (27) and (28), based on the inductance and resistance of the generator, and the desired response bandwidth α , in rads/s, and aims to give a first-order step response with no overshoot. Response speed is limited by the controller delay, with the maximum bandwidth with no overshoot, α_c , given by (29), where t_{cd} is the controller time delay. In general, the time delay will be around 1.5 times the sampling period – one sampling period between ADC sampling and application of the calculated duty cycle, and an additional half period from the

modulation. For the sampling rate of 5kHz, a maximum bandwidth of 1,140 rads/s can be achieved, and the controllers are tuned for 1000 rads/s or 162Hz to be conservative.

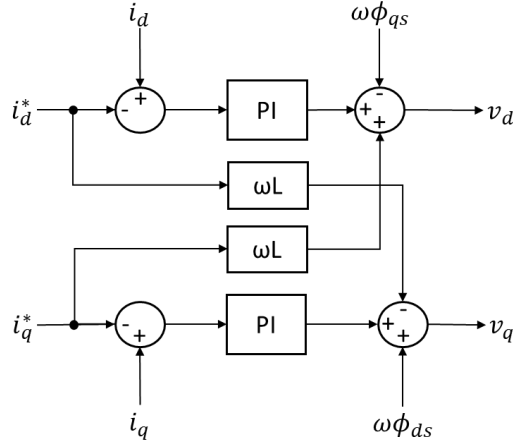


Figure 13 Generator current controller structure

$C(s) = K \left(1 + \frac{1}{sT_i} \right)$	(26)
$K = \alpha L$	(27)
$T_i = \frac{L}{R}$	(28)
$\alpha_c = \frac{6 - 4\sqrt{2}}{t_{cd}}$	(29)

Of course the damper and field windings cannot be ignored, so for the tuning of the PI controllers and cross-coupling terms inductances based on the transient and subtransient reactances are used. These reactances are calculated based on the parallel combinations of the mutual reactance and the field and damper leakage reactances, in series with the stator leakage reactance, and govern the electrical behaviour over short time scales.

The q-axis transient reactance, X'_q , is given by (30) while the d-axis subtransient reactance, X''_d , is given by (31). The mutual reactance, $X_{md,q}$, is given by (32). The q-axis subtransient reactance is not defined, as the 5th-order model used for the salient-pole generator does not include a second damper winding in the q-axis. Using the generator parameters in Table 2, X'_q is found to be 0.2 and X''_d is 0.216. For simplicity, the same parameters are used for the d- and q-axis controllers, based on a reactance of 0.2 per-unit.

$X'_q = X_{ls} + \frac{X_{mq}X'_{lkq}}{X_{mq} + X'_{lkq}}$	(30)
$X''_d = X_{ls} + \frac{X_{md}X'_{lfd}X'_{lkd}}{X_{md}X'_{lfd} + X_{md}X'_{lkd} + X'_{lfd}X'_{lkd}}$	(31)
$X_{md,q} = X_{d,q} - X_{ls}$	(32)

The tuning defined in (27) and (28) was found to provide the expected rise time for the current, but resulted in an initial error in the current due to the interactions between the generator

windings. Manually increasing the integral gain allowed the error to be reduced significantly but not eliminated.

It is also necessary to regulate the generator field current, which controls the d-axis flux. The generator has a relatively low q-axis synchronous reactance, so it is less important to increase the flux at higher loads to support the terminal voltage. Instead, the d-axis stator flux is regulated to be kept constant as it is opposed by the d-axis stator current. For a desired stator flux linkage ϕ_d^* , the required field current referred to the stator, i'_{fd} , is given by (33). In the generator model, the per-unit field current is defined such that 1 per-unit current will provide the rated terminal voltage at zero load, so the field current can be defined as $i_{fd}^* = i'_{fd} L_{md}$, and the field current demand is given by (34). A PI controller is used to regulate the field current through the field voltage, with the model defining 1 per-unit voltage as that which will provide 1 per-unit current in the steady state. A relatively slow tuning was used, which was carried out by hand.

$i'_{fd} = \frac{\phi_d^* - L_{ls}i_d}{L_{md}} + i_d$	(33)
$i_{fd}^* = \phi_d^* + (L_{md} - L_{ls})i_d$	(34)

An example of the simulated generator torque control is shown in Figure 14, in which the generator speed is kept constant at 1pu, and the generator-side converter feeds a constant DC voltage. Field current is increased at a relatively slow rate to maintain the d-axis flux. A closer look at the torque and current is shown in Figure 15, showing the fast torque control response, with a small initial error which is eliminated over the course of around 0.1s. Parameters for the controllers are given in Table 7.

Table 7 Generator-side controller parameters

Stator current controller proportional gain	0.65
Stator current controller integral gain	10
Field current controller proportional gain	20
Field current controller integral gain	20
Sampling frequency	5kHz

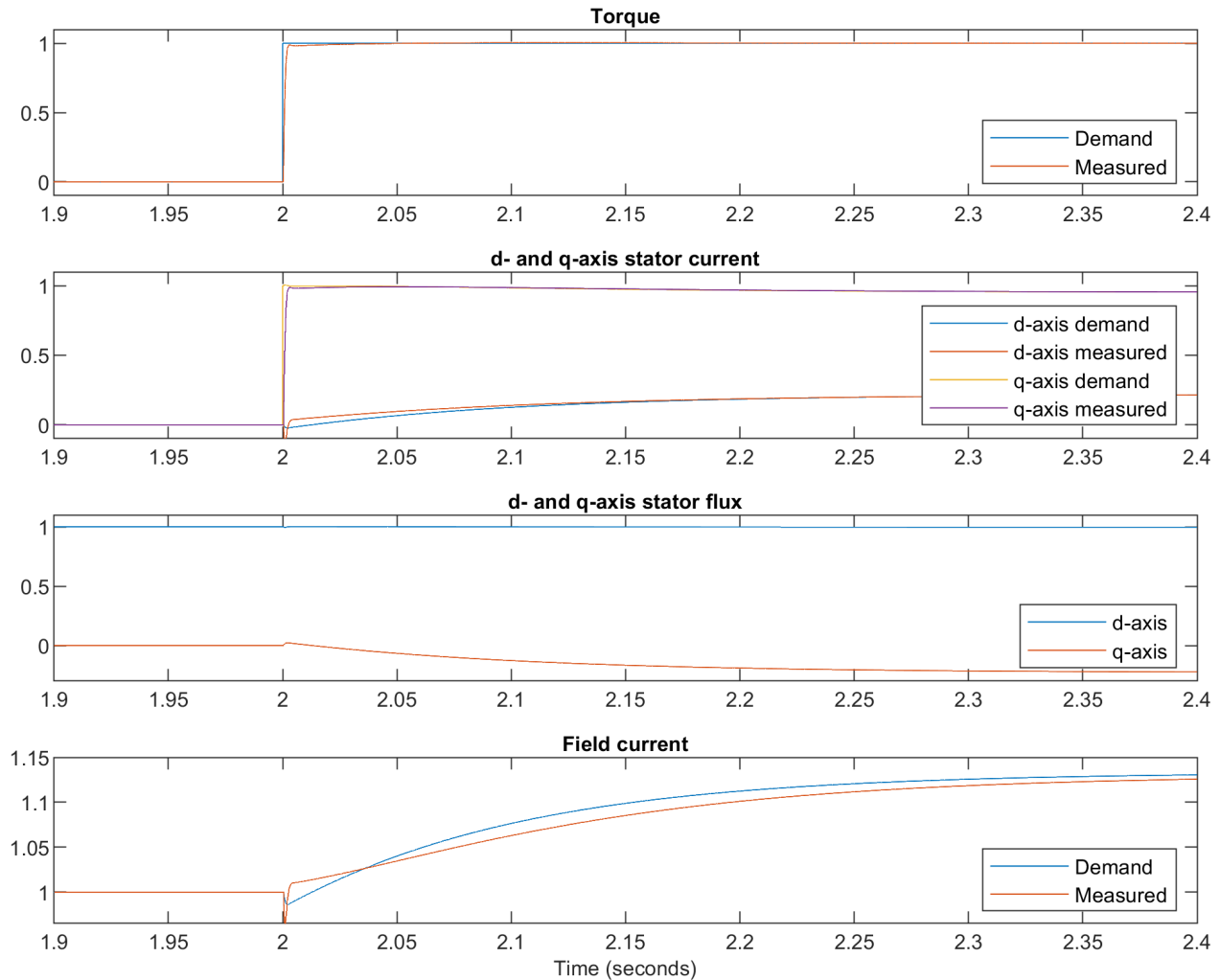


Figure 9 Generator torque and field control

3.5 Grid-side control, virtual synchronous machine

A significant reason to implement variable speed hydropower is to increase the flexibility of the electrical grid, to compensate for an increased proportion of inflexible converter-connected generation, such as wind and solar power. A downside of this is that placing the existing generator behind a converter further reduces the inertia of the grid, so it is desirable to provide some sort of synthetic inertia. Provision of synthetic inertia by wind turbines is under investigation, but potentially has problems when the requirements of the synthetic inertia controller conflict with the turbine controller, causing damaging mechanical loads (Henderson, Vozikis, Holliday, Bian, & Egea-Álvarez, 2020). It is therefore preferable to provide the virtual inertia using the real inertia of the synchronous generator present in the hydropower plant.

The simplest method to provide synthetic inertia is to modify a conventional vector current controller with an additional term, which modifies the current demand based on the rate of change of grid frequency. Problems with this approach are that it relies on differentiating the grid frequency measurement, which is prone to issues with noise, and relies on a phaselock loop (PLL) for grid frequency measurement, with all the problems this can cause in weaker grids.

Fundamentally, it is still a grid-following controller, and relies on the presence of synchronous generators on the grid which it can follow.

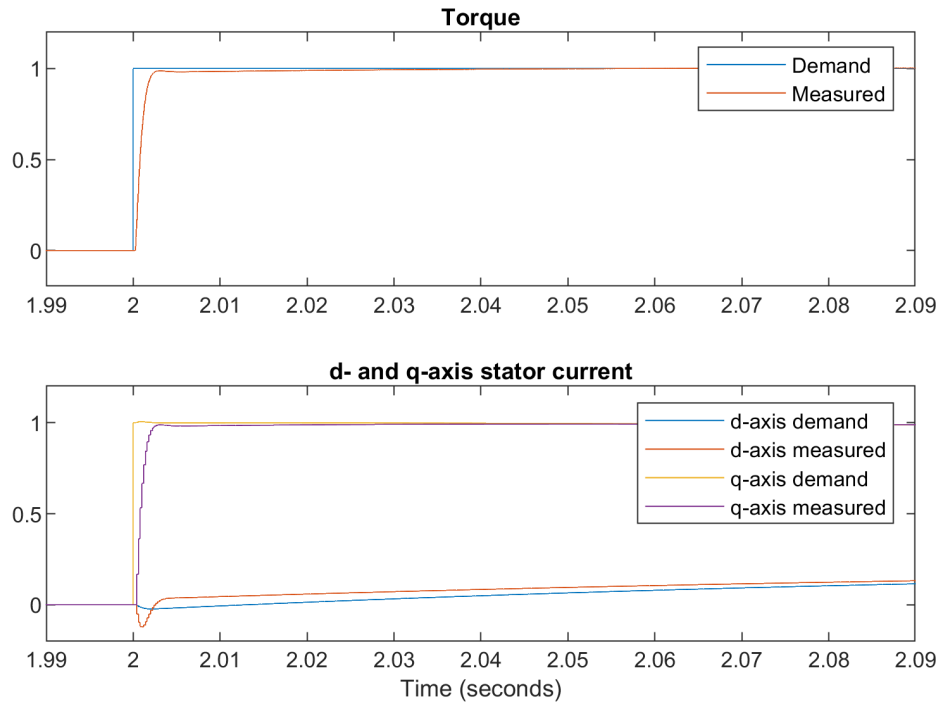


Figure 10 Generator torque control detail

The virtual synchronous machine (VSM) solves these problems by emulating the characteristics of a synchronous machine, and is classified as a grid-forming controller. It has been proposed with a low virtual inertia as a solution for controlling converters in a weak grid, and with higher virtual inertia for the provision of synthetic inertia services, and the latter approach is most relevant for this application. The VSM has the following potential disadvantages:

- Difficulty in limiting the converter current – unlike a real synchronous machine, a converter cannot handle large overcurrents, so additional systems to limit the current must be implemented.
- Difficulty in handling severe grid faults, which is partly related to the first problem.
- Slow response if a significant inertia is emulated.

Because of these issues, the grid-side converter controller will also include a conventional vector current controller and PLL, which will be activated during grid severe faults. It will also operate when the turbine is not generating, and the converter DC link voltage is regulated from the grid-side converter, requiring a faster response speed.

This section will first briefly describe the conventional vector current controller, then introduce the virtual synchronous machine and finally show how the two controllers are integrated.

3.5.1 Vector current controller

The overall structure and connection of the vector current controller is shown in Figure 16, with the current controller itself shown in Figure 17. The PLL locks to the grid voltage, and allows the grid voltage and current, v_{abc}, i_{abc} , to be transformed to a d-q rotating reference frame with the d-

axis aligned to the grid voltage vector. This is different from the generator converter, in which convention dictates that the d-axis is aligned to the rotor field.

The current controller is tuned with the internal model method, to achieve a control bandwidth of 100Hz. It produces a converter voltage $v_{cd,q}$, which is converted back to the fixed reference frame and modulated for the converter. A phase delay ωt_{cd} is added to reference angle for the conversion to the fixed reference frame, which compensates for the time delay between the measurement of the current and voltage and the application of the new duty cycle, plus the effects of the modulation. This reduces cross coupling between the d- and q-axis controllers as well as reducing steady-state errors which must be compensated by the integral part of the current controllers.

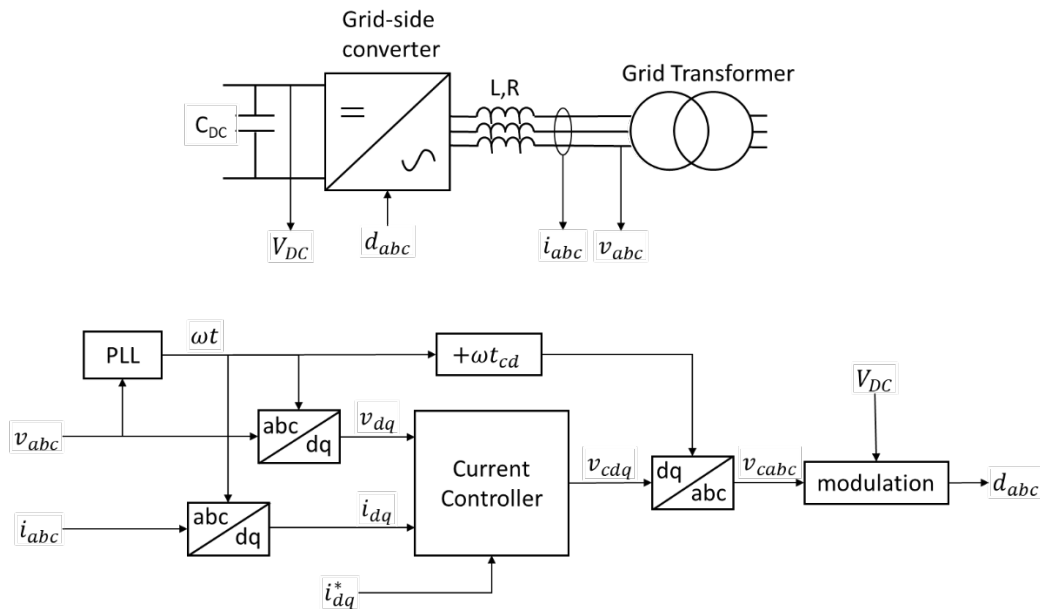


Figure 11 Current controller connection

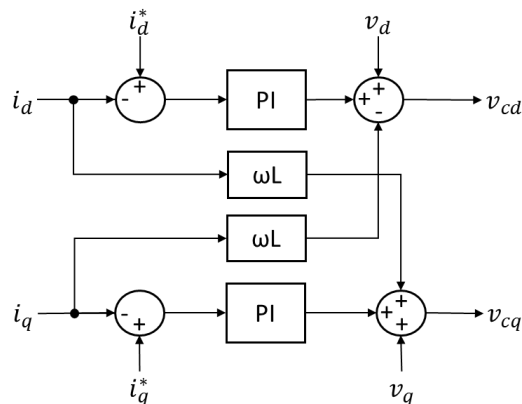


Figure 12 Current controller structure

An important point to note is that with the cross-coupling terms in the current controller, and with the time delay compensation, the main role of the integral part of the current controller is to compensate for the resistance of the coupling inductor. Thus the integral part of the controller

can be disabled with only minor steady-state errors introduced, and this will become important later when the virtual synchronous machine is integrated.

3.5.2 Virtual synchronous machine

The overall structure of a typical virtual synchronous machine implementation is shown in Figure 18. The measured voltage and current, v_{abc}, i_{abc} , are used to calculate the instantaneous real and reactive power, P, Q , using (35) and (36). The virtual synchronous machine and virtual excitation blocks then produce the reference angle ωt and magnitude $|V|$ for the three-phase voltage applied to the converter, v_{cabc} , which is modulated as before. The virtual excitation simply regulates the reactive power through the voltage magnitude using a PI controller, but the VSM requires more explanation.

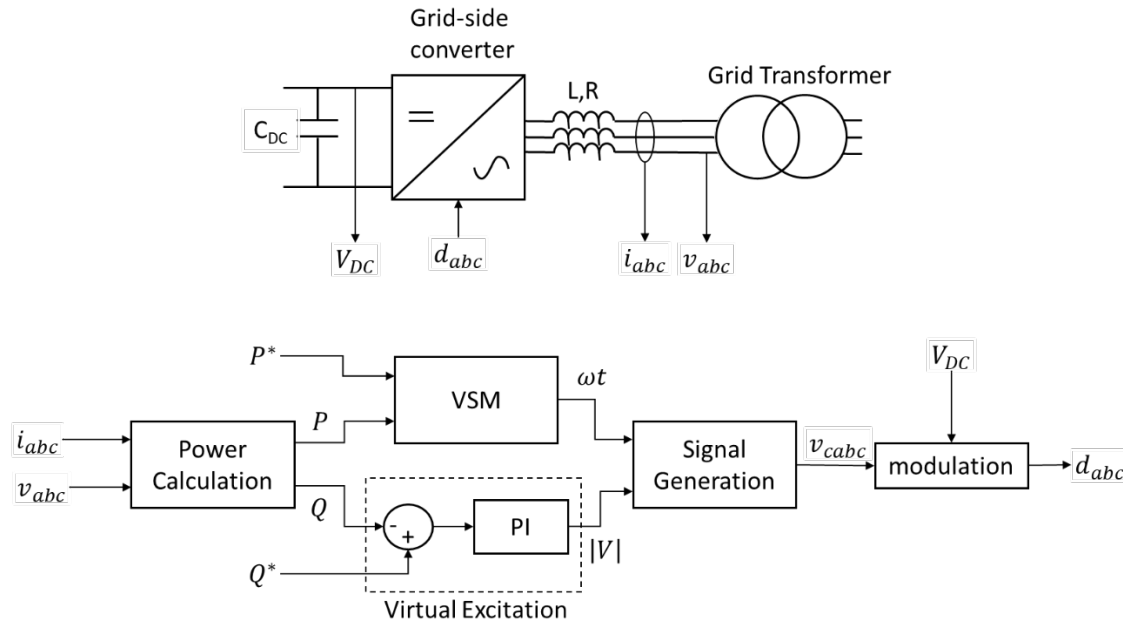


Figure 13 Virtual synchronous machine controller connection

$P = v_a i_a + v_b i_b + v_c i_c$	(35)
$Q = \frac{1}{3} (i_a (v_b - v_c) + i_b (v_c - v_a) + i_c (v_a - v_b))$	(36)

Synchronous machine dynamic performance is governed by the swing equation (37), where P_m is the per-unit mechanical power input, P_e is the per-unit electrical power output, ω_s is the synchronous speed of the grid and H is the inertia constant of the generator. δ is the load angle between the generator electromotive force (EMF) and the grid voltage vector. Based on this, the reference angle ωt for the VSM could be derived using (38), which differs in that ωt is an absolute angle and therefore continually integrating while δ remains constant for a steady power output, but leads to the same performance. Directly emulating δ would entail measuring the angle of the grid voltage vector using a PLL, defeating part of the purpose in using a VSM.

$\frac{2H}{\omega_s} \frac{d^2 \delta}{dt^2} = P_m - P_e$	(37)
---	------

$$\omega t = \frac{\omega_s}{2H} \iint P^* - P dt \quad (38)$$

Such a method would not work well as it lacks any damping – the power output would continuously oscillate. Real synchronous generators include damper windings, which apply a force based on the rate of change of load angle, but as load angle is not emulated directly such a system is more difficult to apply. One option is to apply a virtual force based on the difference between the virtual generator speed and the rated synchronous speed, but this has the effect of adding a frequency droop characteristic to the VSM (D'Arco & Suul, 2013). While it is intended to include such a system for frequency support, it is desirable for it to be separate from the VSM – in a real generator the frequency droop control is related to the prime mover governor.

Instead, the first integrator in (38) is replaced with a PI controller, with the integral gain set as in (38), which outputs the virtual generator speed ω , as shown in Figure 19. This is then integrated to produce the angle reference ωt . The proportional gain K_P determines the damping of the VSM, and this can be much higher than would occur in a conventional synchronous machine, which would be limited in the amount of damper windings that can be fitted.

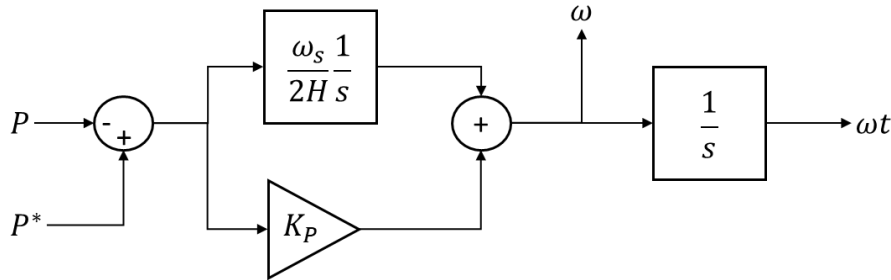


Figure 14 VSM angle reference

A comparison of the real and virtual inertia is shown in Figure 20, where the VSM trace comes from the virtual synchronous machine controller, with power rating 325MW and an inertia constant of 6.5s, and the SM trace from a grid-connected synchronous machine with identical parameters. The VSM uses a proportional gain of 10. At time 30s, the frequency ramps from 50Hz to 49.5Hz over 2s. It can be seen that the additional power and energy released by the VSM is identical to that of the SM, but with a lower level of oscillation. The increased damping leads to a slightly lower initial energy release.

3.5.3 Controller integration

Integration of the vector current controller and the VSM is achieved using a similar method to that used in the power synchronisation controller, which is a grid-forming controller related to the VSM but with some differences in the derivation of the angle reference (Zhang, Harnefors, & Nee, 2010). The structure of the integrated controller is shown in Figure 21, with the vector current controller appearing at the top and the modified VSM at the bottom. There are now two grid frequencies – ω_G is the grid frequency measured by the PLL, while ω_V is the frequency of the VSM.

A significant change in the VSM operation is that the voltage reference, v_{vdq} , is now generated in the d-q reference frame provided by the PLL as an intermediate step. A resonance damping block

is also included to damp high frequency resonances that occur naturally in VSM systems, this implements a virtual resistance with a first-order high-pass filter, and is shown in Figure 22.

Key to the integration of the controllers is the anti-current controller. As stated previously, the current controller exhibits only small steady-state errors when the integral component is not used, and while the VSM is operating the integrators are disabled. In this situation, the output of the current controller, v_{cdq} , depends directly on the inputs, v_{dq} , i_{dq} and i_{dq}^* . The purpose of the anti-current controller is to generate a current reference i_{vdq}^* such that the output of the current controller will equal v'_{vdq} . As this value is passed through a limiter, the current controller will still be capable of limiting the current if necessary. The anti-current controller is shown in Figure 23.

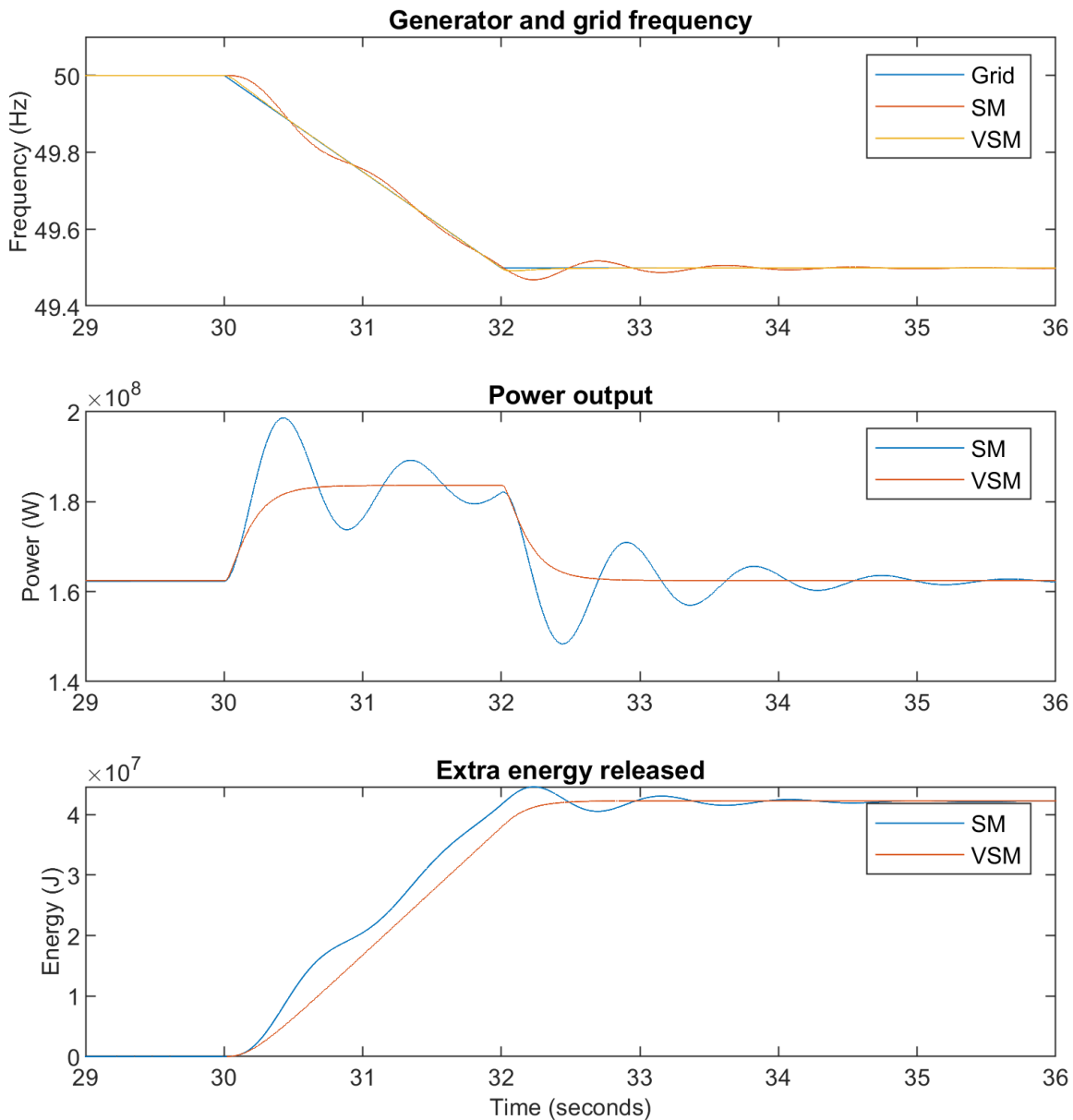


Figure 20 Comparison of real and virtual inertia

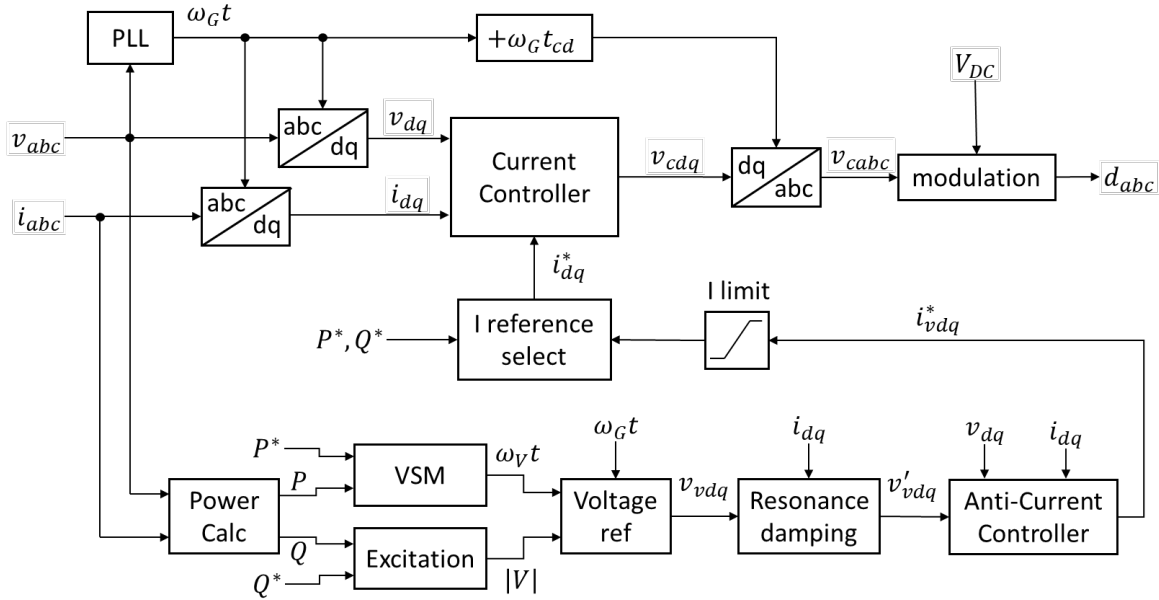


Figure 21 Integrated current controller structure

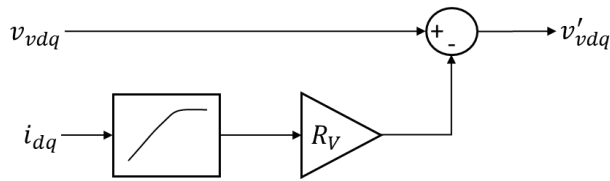


Figure 22 Resonance damping controller

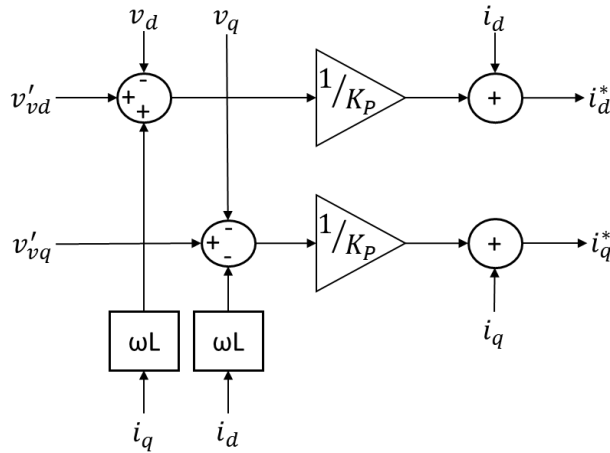


Figure 23 Anti-current controller

When operating without the VSM, the d- and q-axis current references are calculated by dividing the real and reactive power references by a filtered value of the measured grid voltage magnitude. Not shown in Figure 21 is the block for setting the initial conditions of the VSM and Virtual Excitation blocks. These set the integrators such that when the VSM is activated, the reference voltage will be equal to the previous output from the current controller, meaning that transition to VSM operation will be seamless.

Transition between vector current controller and VSM operation while generating is shown in Figure 24, in which the VSM is activated at 5s and de-activated at 6s. Activating the VSM has no effect on the current, but shows an increase in the d-axis current demand and a minor decrease in the q-axis. This is due to the VSM taking up the values of the current controller integrators as initial conditions, which affect the output of the anti-current controller – the change is instantaneous and has almost no effect on the measured current. When transitioning to the vector current controller, the current controller integrators are zeroed, so there is a current transient in the d-axis. This also causes a transient in the angular velocity reference, affecting the q-axis current – while the VSM is active this reference comes from the VSM, otherwise it comes from the PLL. Transition to vector current control operation is only likely to occur during grid faults, where this effect is likely to be buried underneath more significant transients.

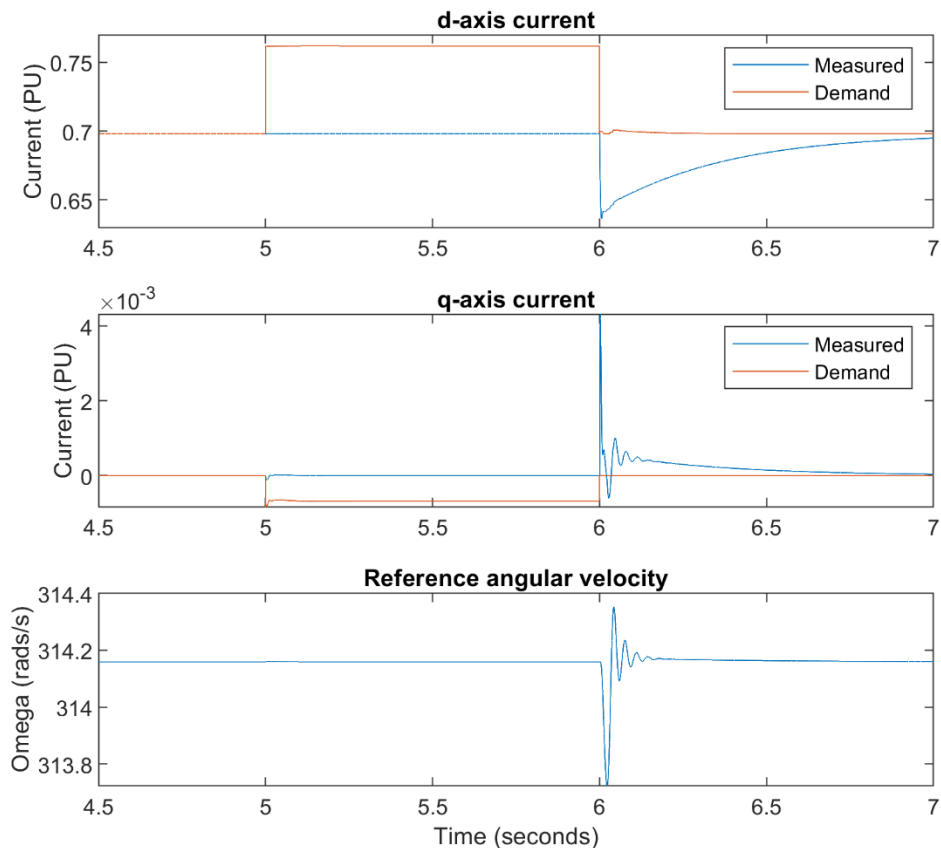


Figure 15 Activation of VSM

Operation of the current limiting function is shown in Figure 25, in which a voltage dip to 80% of the nominal value is applied at 10s, lasting for 0.5s. As can be seen, the current is successfully limited during the initial transient and during recovery. It should be noted that the limit value is slightly below the limit set in the controller of 1PU. This is due to the additional d-axis current demand to compensate for the voltage drop across the resistance of the grid coupling inductor, as also seen in Figure 24, so this would need to be compensated for when setting the limit.

Another factor to notice is the worst performance of the angular velocity reference during recovery when the current limit is applied. This is due to the reference angular velocity winding up due to the current limit, as the decreased virtual load angle is having no effect on the power

transfer, and a more significant voltage dip will cause the VSM to lose synchronisation. Modifications to the controller may help with this issue, but in often VSM systems fall back on a vector current controller during voltage dips.

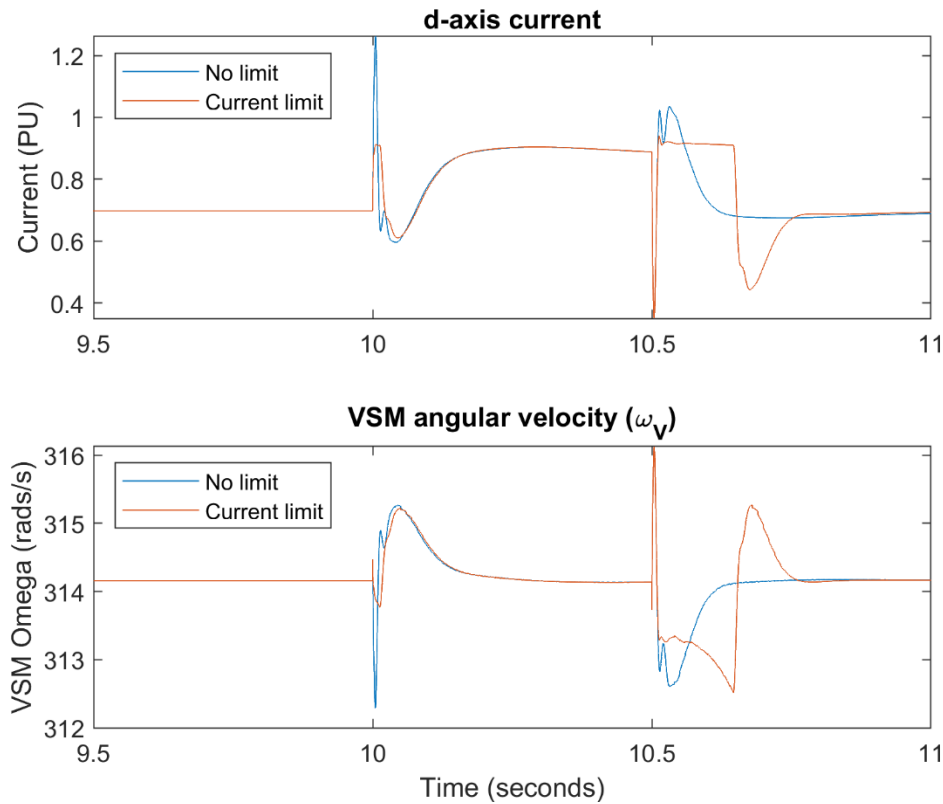


Figure 16 Operation of current limiting

3.5.4 Grid-side controller parameters

Current controller proportional gain	0.2
Current controller integral gain	0.63
Current controller bandwidth	100Hz
Virtual inertia constant	6.5s
VSM proportional gain	5
Virtual excitation proportional gain	0.1
Virtual excitation integral gain	10
HF damping virtual resistance	0.1
HF damping cutoff frequency	5s
Sampling frequency	5kHz

3.6 DC-link voltage controller

The DC-link voltage controller can take two different structures depending on the state of the system. When the generator is not ready, for instance if it is stopped or being run up to operating speed, the DC-link voltage is controlled by a PI controller which sets the power demand for the grid-side converter. In normal operation, with the generator running, the frequency support controller sets the power demand for the grid converter, while the DC-link voltage PI controller

sets the power demand for the machine-side converter, using the grid converter power as feedforward. These arrangements are shown in Figure 26.

The settings for the DC-link voltage controller are given in Table 8. As can be seen, the controller integral gain is currently set to zero – adequate performance is achieved using just the proportional gain and feedforward. In a more accurate converter model, which properly represents the converter losses, some integral gain will be required to compensate for the difference in power transfer of the two converters.

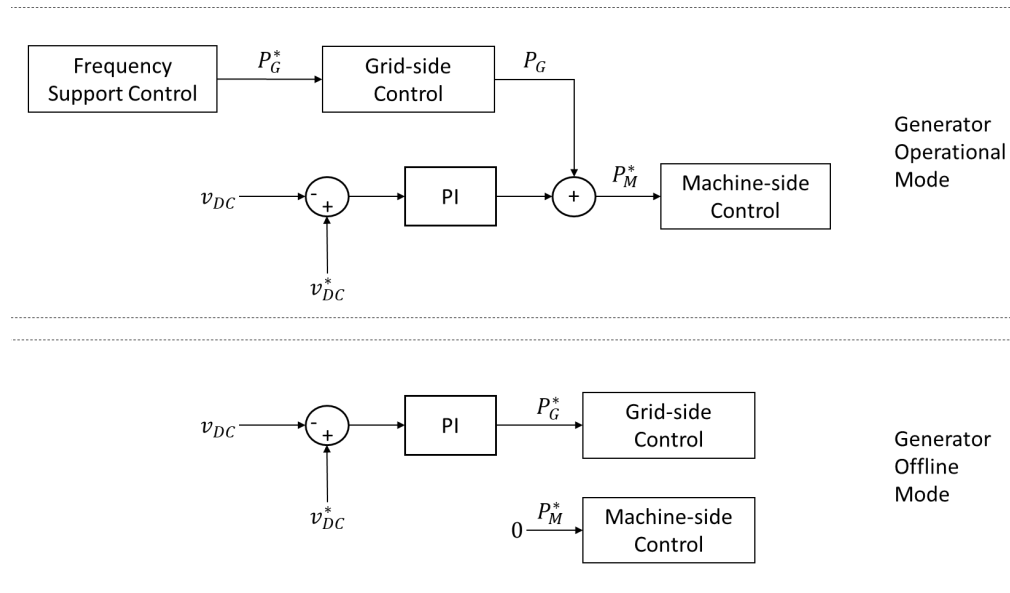


Figure 17 DC-link voltage controller structures

Table 8 DC-link voltage controller settings

Voltage controller proportional gain	1
Voltage controller integral gain	0
Sampling frequency	5kHz

3.7 Frequency support controller

The purpose of the frequency support controller is to regulate the grid power to fulfil the grid code requirements for provision of frequency support services, while preventing the turbine from entering any damaging operating modes. The main frequency support services, as defined in the GB grid code, are as follows (National Grid Electricity System Operator Limited, 2020):

- Primary response, which reaches the required amount within 10s of a drop in the grid frequency, and is sustained for no less than 20s.
- Secondary response, which reaches the required amount within 30s of a drop in the grid frequency, and is sustained for up to 30 minutes.

Both of these are governed by a frequency droop control, providing extra power proportional to the drop in frequency, down to a limit of -0.5Hz below nominal, and the generator must be able to offer an increase of at least 10% of rated power. A deadband of $\pm 0.015\text{Hz}$ around the nominal is

allowed. The grid codes of other nations have similar definitions of primary and secondary response, and differ mainly in the market mechanisms with which these services are tendered.

In addition to the optional frequency support services, for which the generator will receive an additional payment, there is a mandatory requirement to reduce power output in the event of the grid frequency being above the nominal value, and this is governed similarly to secondary response. An additional related service is fast start, in which a generator is paid to be able to rapidly start from a standby condition, and this is another area where variable-speed hydropower can provide an advantage and will be considered in this section.

3.7.1 Operating limits

Limits in on the operating region of the turbine while generating are as follows (Mercier, Olivier, & Dejaeger, 2016):

- Minimum power limits for a given speed – combinations of a low discharge speed associated with a low power output with a high turbine speed will lead to excessive swirl in the discharge tube of the turbine. This leads to cavitation, and ‘vortex rope’ formation, causing operational stability. There is also a maximum power limit through a similar mechanism.
- Maximum and minimum turbine speeds, to prevent high angles of attack on the runner blades leading to cavitation and blade damage.
- Current limits in the generator and converter. These are most relevant when attempting to draw close to rated power at lower generator speeds, it is expected that the generator can tolerate this for a short period while the converter will need to be rated to handle the expected transient current.

Of these limits, the second is most significant for the controller, as borrowing energy from the turbine rotor to provide fast frequency response will naturally slow it down, and risk blade damage if the speed drops too much. In general, a speed range of $\pm 30\%$ of nominal could be allowed (Iliev, Trivedi, & Dahlhaug, 2019). The limit extends above the nominal speed, providing an allowance for overspeed during a loss of grid event. It has been suggested that this could be used to increase the operating speed of the turbine, providing more energy storage in the inertia, as dump resistors could be used to limit the turbine speed during a loss of grid (Iliev, Trivedi, & Dahlhaug, 2019). This is not considered in this study, as sustained operation of an existing generator and turbine above rated speed could have other undesirable effects, but may be a useful consideration in a new installation.

The swirl cavitation limit has greater significance in the selection of the setpoints for steady-state operation, in that lower power outputs will require a slower turbine speed to reduce the discharge tube swirl. This places limits on the available frequency response capability, as the turbine will be operating closer to the lower speed limit, with less usable stored energy in the inertia.

3.7.2 Controller structure

The change to power demand is calculated using the system shown in Figure 27, which first calculates the difference between the grid frequency F_G measured by the VSM, and the nominal frequency F_N , and applies the deadband. The high frequency and secondary responses are calculated using droops K_{HF} and K_{Sec} , and passed through a low-pass filter then added. The

primary response is calculated using droop K_{Pri} , and in addition to a low-pass filter, a 20s time delay is used to limit the time which the primary response is applied. The primary response signal is kept separate from the secondary and high frequency responses as these are treated differently in the power-limiting section.

Two power limits are calculated, P_{Lim1} and P_{Lim2} , as shown in Figure 28. P_{Lim1} is designed to prevent the turbine from stalling due to the power demand being higher than the maximum available at the current speed, with guidevanes at maximum opening. This is accomplished using a lookup table based on the turbine speed ω , and an additional droop gain K_{L1} further lowers the power demand based on the difference between the turbine speed and its setpoint ω^* , which allows some power to re-accelerate the turbine to the setpoint. P_{Lim2} is designed to prevent the turbine speed dropping below the minimum, and provides a linear decrease in power as the speed drops below a setpoint, with the rate dependant on the droop gain K_{L2} .

The power references for the grid converter P_G^* , and governor feedforward P_{FFD} are calculated according to the quantities above using the structure shown in Figure 29. The basic principle is that P_{Lim2} represents an absolute limit to the grid power, to prevent the turbine dropping below the minimum speed, while P_{Lim1} only applies to the secondary response, allowing a larger primary response than the steady-state power capability.

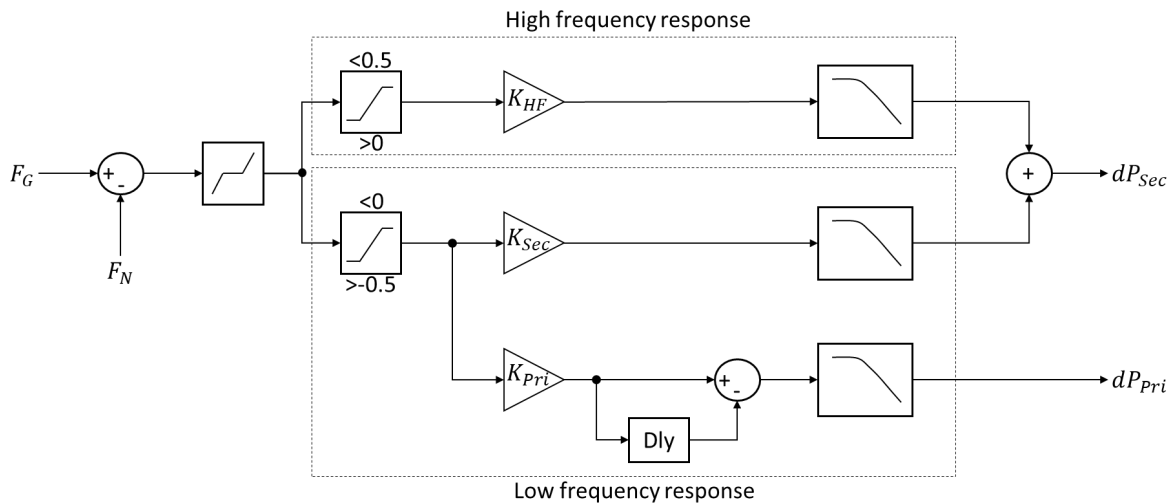


Figure 18 Power change calculation

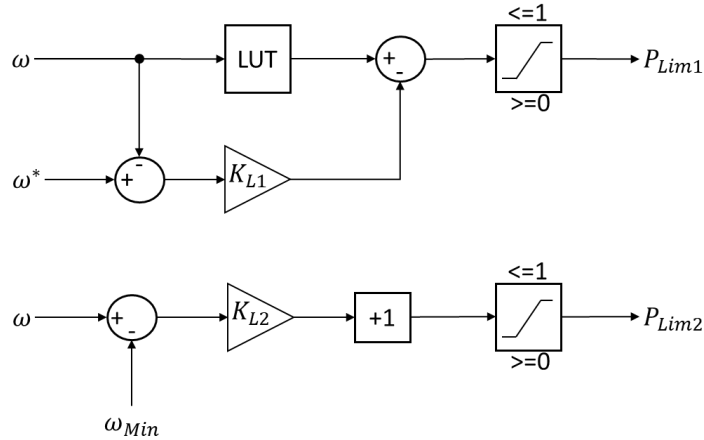


Figure 19 Power limit calculations

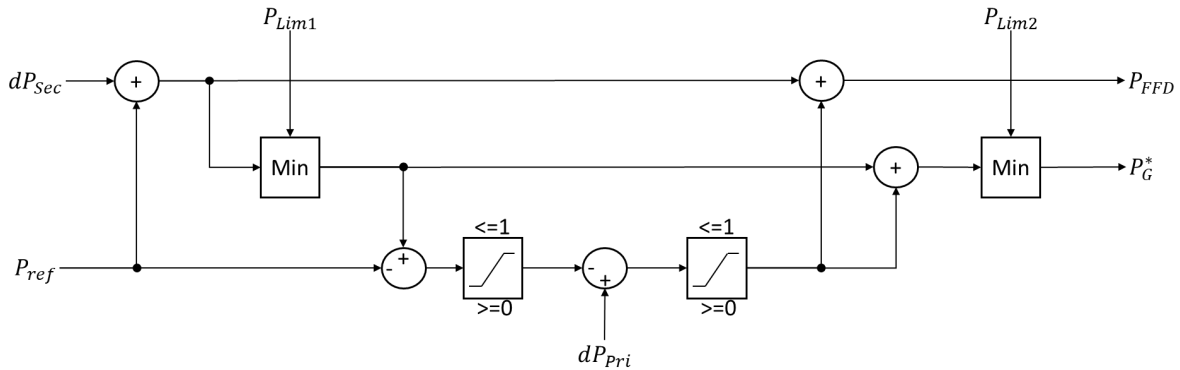


Figure 20 Power reference calculation

3.7.3 Example controller operation

An example of the operation of the frequency support controller, along with the other controllers, is shown in Figure 30, which shows the reaction to a drop in grid frequency from 50Hz to 49.5Hz over 5s. Primary and secondary droops are both set to 0.2PU per 0.5Hz, with a frequency droop limit of 0.5Hz. Steady-state power setpoint is 0.65PU, and the generator speed setpoint is 1PU.

The primary response is provided using the inertia of the turbine, resulting in a drop in the turbine speed. This is slowly recovered after the primary response ends, but is limited as the new operating point is above the maximum power output and the guide vanes are already fully open. These settings are relatively aggressive, and are based around producing a strong primary response. The grid power output can be seen to exceed the demand at the initial frequency transient, which is due to the additional output of the synthetic inertia.

An example of fast startup is shown in Figure 31, in which the turbine is started from standstill with a speed setpoint of 1 and a power setpoint of 0.65. This example shows the influence of P_{Lim2} , which limits the grid power until the turbine has reached the minimum speed, allowing the turbine to rapidly accelerate up to this speed. Following the start of grid power output, P_{Lim1} limits the power, allowing the turbine to accelerate to the operating speed slowly. In fast-start, the advantage of variable-speed operation is that it is not necessary to accelerate the turbine to the

rated speed, and there is no synchronisation step, greatly reducing the time before power is exported to the grid.

3.7.4 Frequency support controller parameters

Parameters used in the frequency support controller are given in Table 9.

Table 9 Frequency support controller parameters

High frequency time constant		0.1s
Secondary response time constant		5s
Primary response time constant		0.1s
Primary response duration		20s
Frequency deadband		0.015 Hz
Frequency limit for droop application		0.5 Hz
Speed recovery droop	K_{L1}	0.5
Minimum turbine speed	ω_{Min}	0.7
Minimum speed droop	K_{L2}	10
Sampling frequency		100Hz

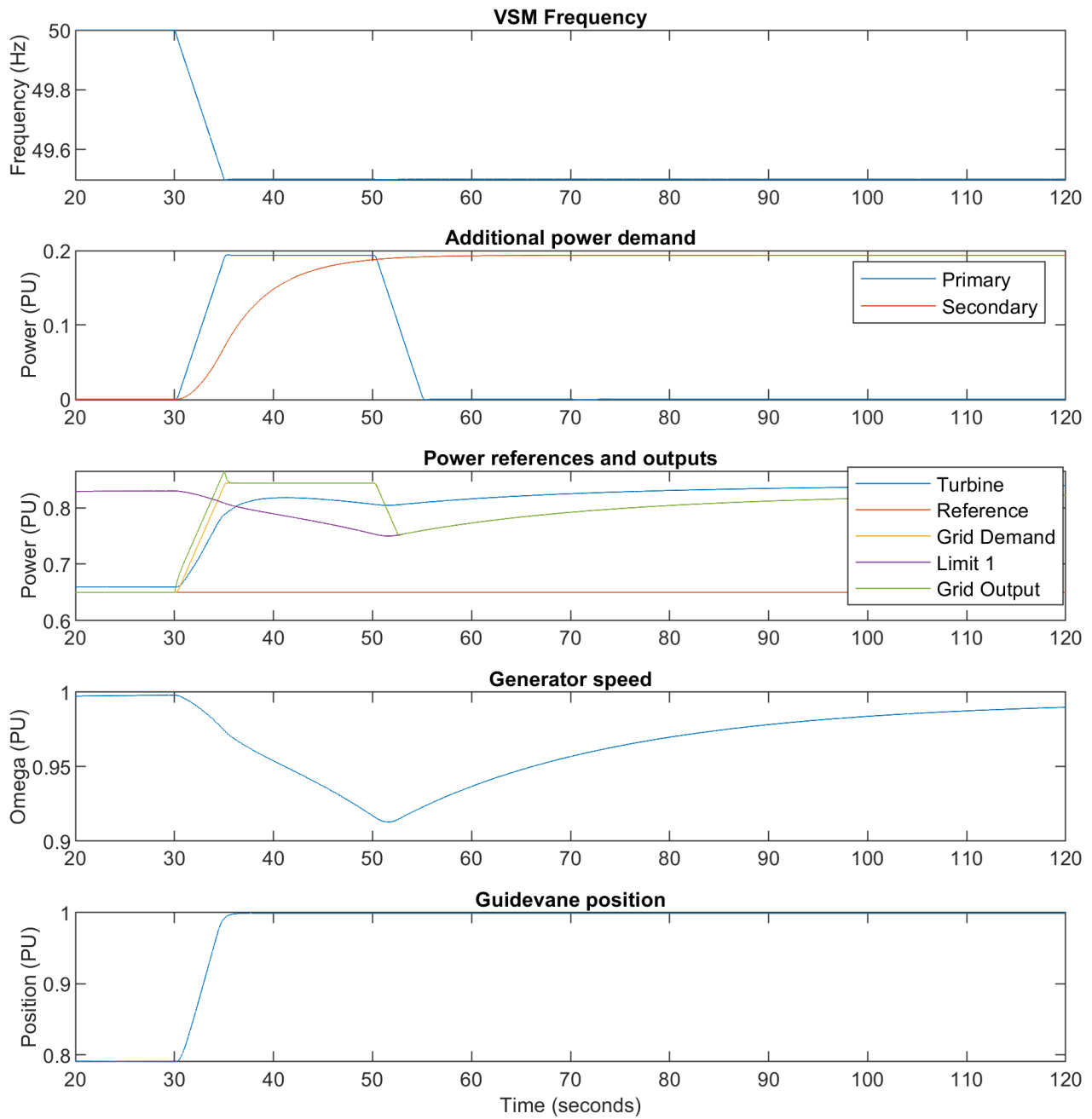


Figure 30 Example of frequency support controller operation

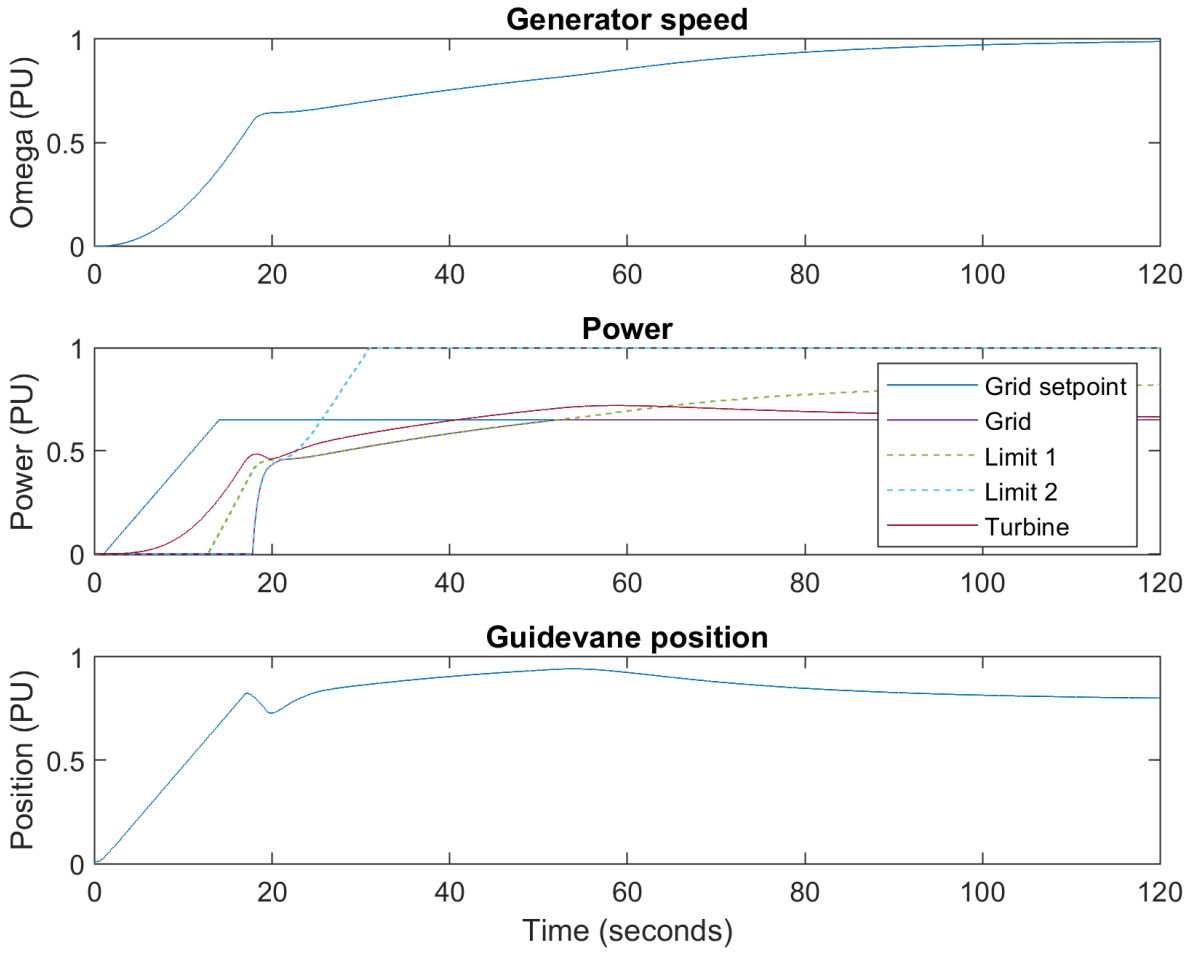


Figure 31 Example of fast start operation

4 Simulated Performance

The model was simulated with two different grids: a stiff grid consisting of a voltage source, resistance and inductance; and the representative grid model introduced in deliverable 4.1.

4.1 Stiff grid

For the stiff grid, a short circuit ratio of 10 is used, along with an X/R ratio of 10.

4.1.1 Synthetic Inertia

Performance of the synthetic inertia provision of the VSM was evaluated by reducing the grid frequency from 50Hz to 49.5Hz over a period of 5s. This was tested at two power levels: 60% of rated power with the generator at rated speed, and 40% of rated power with the generator at 75% of rated speed. The lower speed reduces the speed margin as the controller will start to reduce the electrical power as the generator speed drops below 70%. Several virtual inertias are tested, from 6.5s to 26s, with the former representing the actual inertia of the generator.

Results are shown in Figure 32. Rapid inertial response can be seen, although it is overdamped at higher inertia constants, which could be fixed by reducing the proportional gain of the VSM. The inertial response draws from the turbine and generator inertia, resulting in a dip in generator speed before the governor is able to raise the turbine power to restore the stored energy. Operating at 75% generator speed should result in a significantly higher speed dip, as the total stored energy in the generator and turbine inertia is almost half that at 100% speed, but this is not evident. This is due to the faster response of the turbine mechanical power at the lower power, due to the greater power headroom.

It is clear that significant levels of synthetic inertia can be provided, above that of the generator itself, and this could be useful compensating for a lower overall grid inertia. However, the minimum turbine speed could limit how much inertial response can be provided during more severe frequency dips, and also uses energy that can be used to provide primary frequency response. Balancing the provision of synthetic inertia against primary response would come down to the expected revenue from providing these services.

4.1.2 Frequency Support

Testing of the frequency support capability was carried out at power levels from 50% to 80%, with the latter being close to the maximum due to the efficiency of the turbine and generator. In all cases, a virtual inertia constant of 6.5s is used, and primary and secondary droops of 20% per 0.5Hz are used. The frequency is ramped from 50Hz to 49.75Hz over 2.5s, which should lead to an increase in power output of 10% of rated power. Results are shown in Figure 33.

Up to 70% base power output, the primary and secondary response can be easily achieved at a faster rate than the turbine power can be increased. At 80% base power output, the initial part of the primary response is achieved through drawing on the generator inertia, but the power output reduces as the base power output starts to be limited due to the slowing generator speed. While the generator speed starts to recover, the power output at 30s after the frequency ramp is still 5% below the base power output. In this situation, where the primary response exceeds the rated power output, modifications to the controller could allow a high primary response to be maintained, but this would more significantly reduce the generator speed, resulting in a significant

negative secondary response. Such a response characteristic may still be useful in a grid with limited primary response capability.

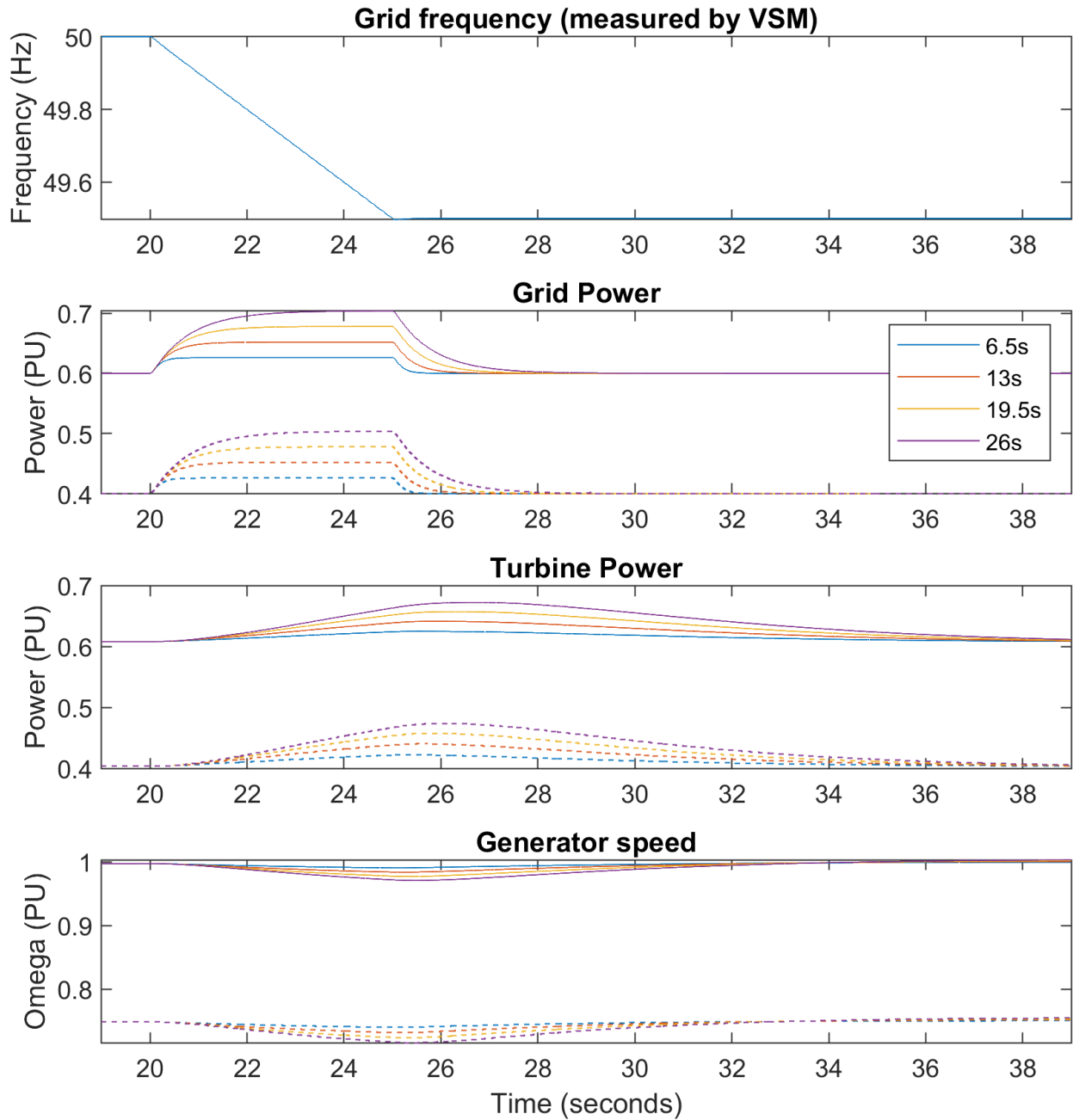


Figure 32 Example of synthetic inertia provision with different inertia constants. Solid lines represent operation at 60% rated power and 100% rated turbine speed. Dashed lines represent operation at 40% rated power and 75% rated turbine speed.

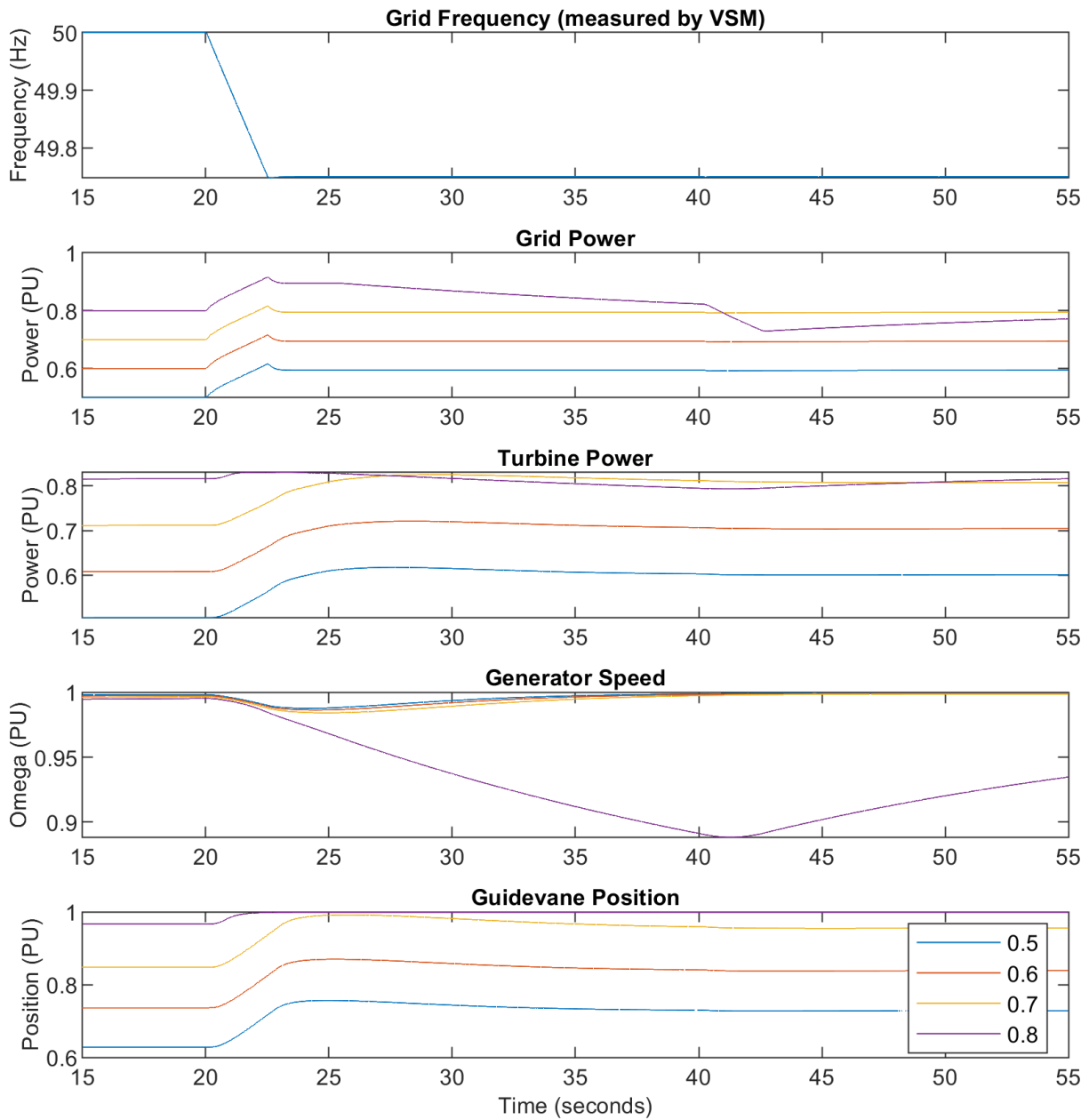


Figure 33 Frequency support provision at different power levels

A comparison with the response of the fixed-speed system is shown in Figure 34, demonstrating the significantly faster response speeds of the variable speed system. As can be seen, much of the slow response speed of the fixed-speed system is due to the governor, due to the transient droop characteristic. Transient droop is required for system stability (Working Group on Prime Mover and Energy Supply Models for System Dynamic Performance Studies, 1992), and the decoupling of the turbine and grid frequencies in the variable-speed system allows for a significantly faster governor response.

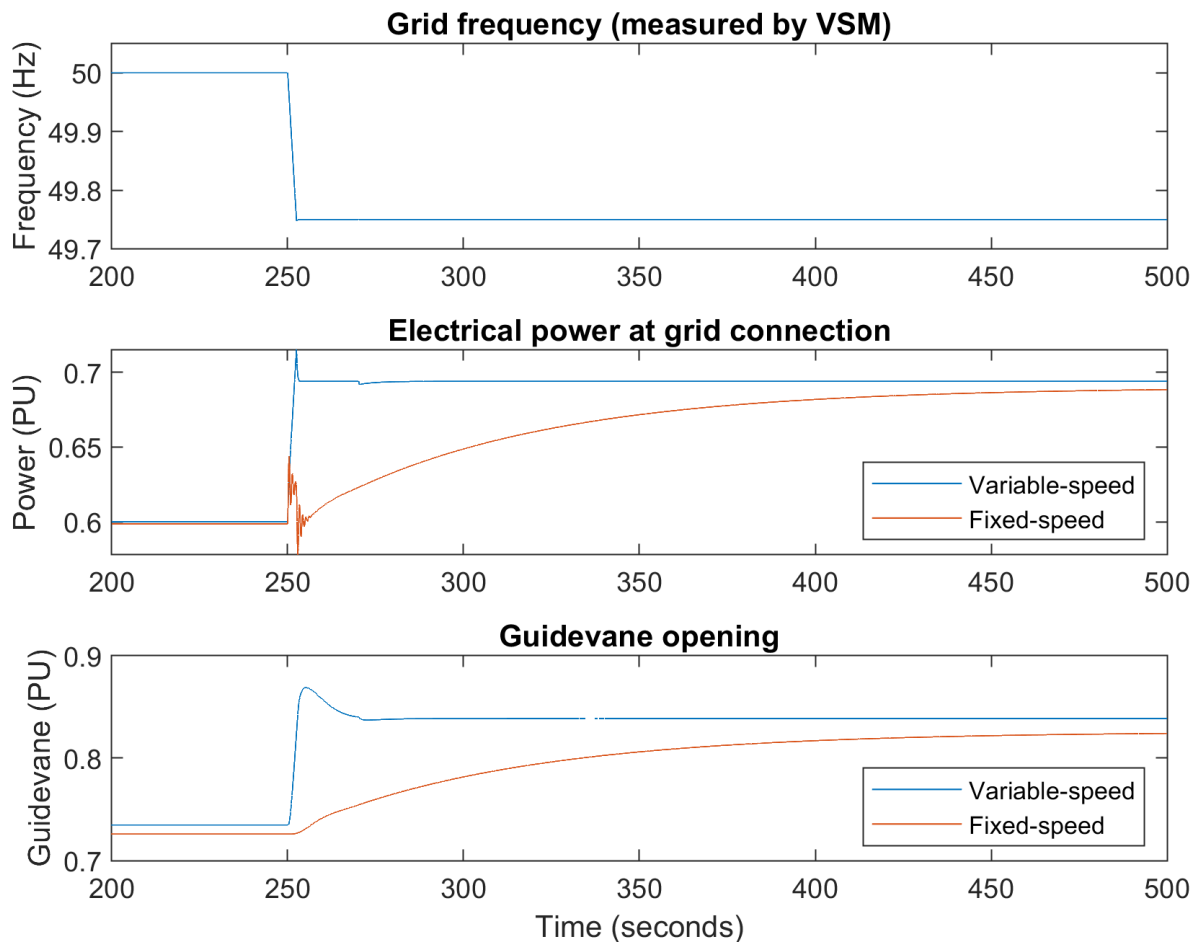


Figure 21 Comparison of frequency support provision with fixed- and variable-speed systems

4.1.3 Over-frequency Response

The response to an increase in grid frequency, with the same parameters as for the frequency dip but increasing from 50Hz to 50.25Hz, is shown in Figure 35.

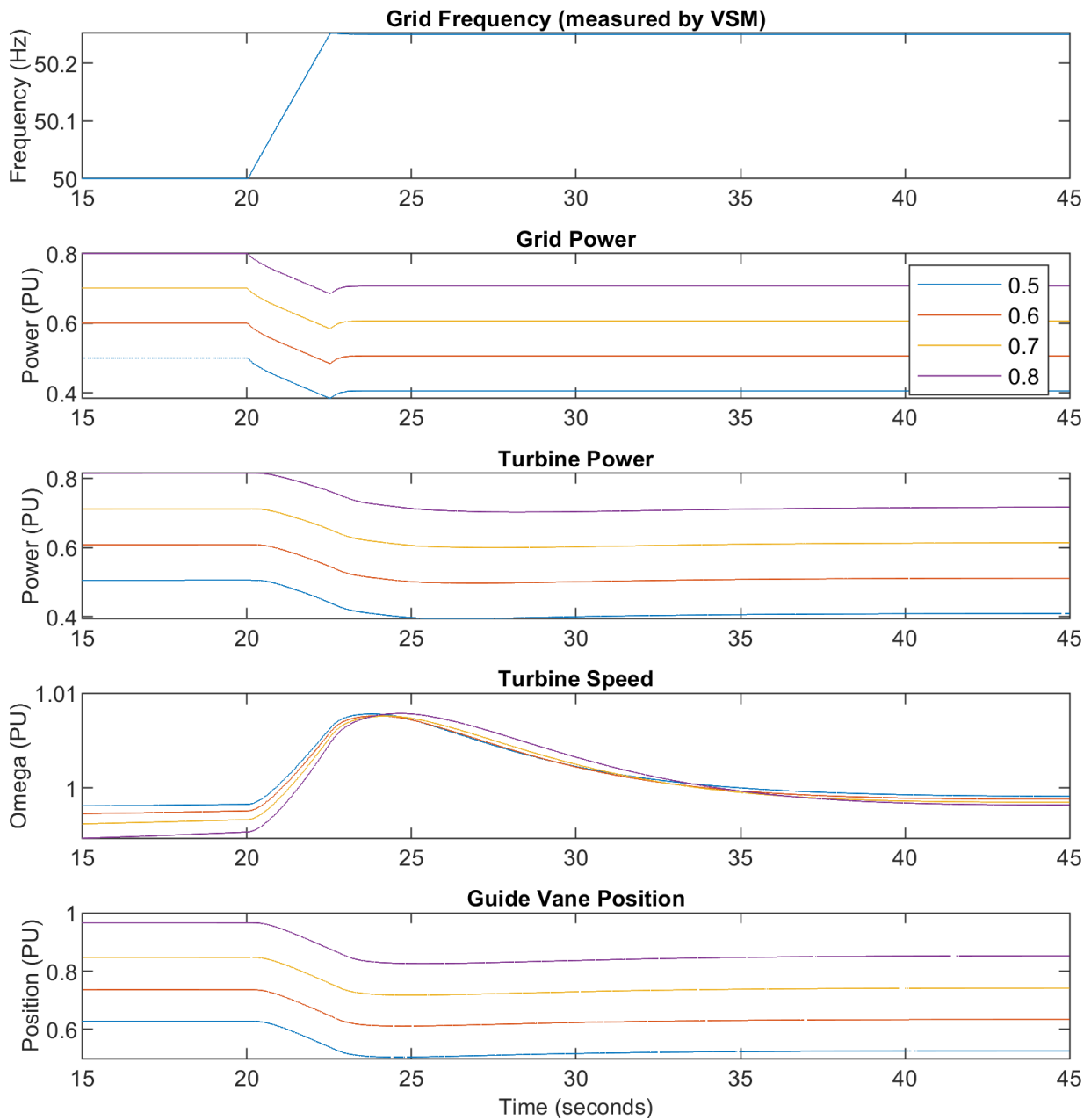


Figure 22 Response to high-frequency event at different power levels

4.1.4 Grid Fault Response

The response of the system to a dip in grid voltage to 50% of the nominal, and lasting for 1s is shown in Figure 36 for the electrical system and Figure 37 for the mechanical, with the mechanical response taking place over a significantly longer timeframe. Base power output is 80% of rated. The particular voltage dip and duration are chosen to create a strong response in both the mechanical and electrical domains. A shorter and deeper voltage dip would cause a greater difficulty for the electrical domain, but would be too short to have much effect on the mechanical.

The VSM deactivates as the measured grid voltage drops below 80% of the nominal, and the d-axis current demand is increased to 100% to allow for maximum real power transfer. Following

recovery of the grid voltage, the VSM is re-activated and power transfer quickly returns to normal. As the converter is operating in real and reactive power control mode, there is no change in reactive power output as there would be if the converter were operating in a grid voltage support mode.

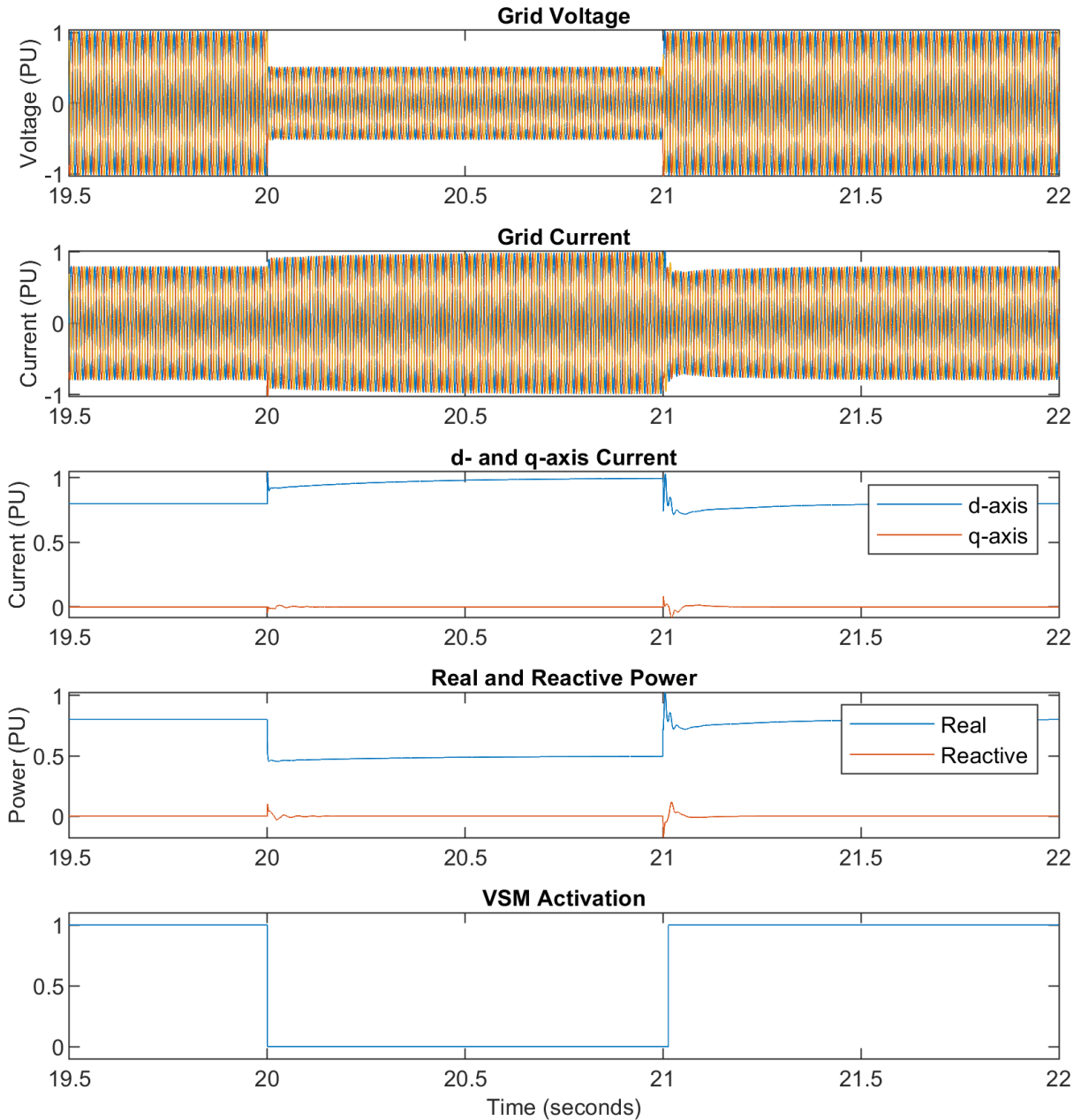


Figure 23 Grid fault ride-through - electrical response

The reduction in power transfer to the grid causes the generator speed to increase slightly, and the governor compensates by reducing the guidevane opening to slow the generator down, which occurs over a relatively long period.

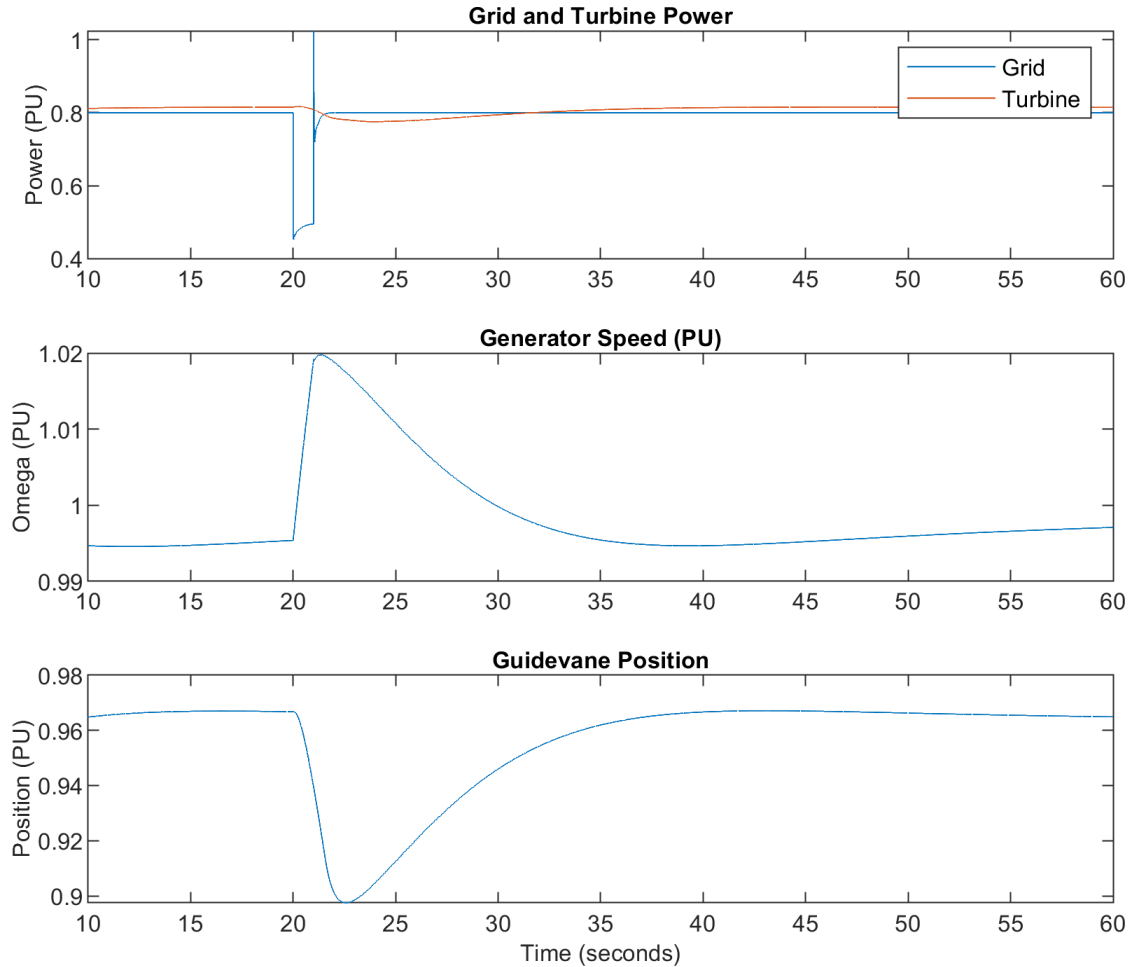


Figure 24 Grid fault ride-through - mechanical response

4.2 With grid model

The grid model is based on the model described in deliverable D4.1, with some modifications, and is shown in Figure 38. In comparison to the original model, station 3 is now inverter-connected, representing a voltage-source HVDC link or wind farm, or a combination of the two, which was done to reduce the system inertia. This station produces a constant real and reactive power, and does not provide any frequency response services. The station uses the same grid-side controller model as the variable-speed hydro plant, with a fixed DC-link voltage, and without using the virtual synchronous machine.

In the test, the line connecting Station 4 is disconnected, with the resulting power imbalance testing the performance of the frequency support provided by the power stations. The test station can be the fixed- or variable-speed hydroelectric plant described earlier in the report, and the variable-speed plant is tested using the virtual synchronous machine controller as well as the conventional vector current controller.

Parameters for the test scenario are shown in Table 10, which is based around having a large hydroelectric capacity available, leading to a significant system inertia. In the models used, the hydroelectric stations have a slow frequency response time in comparison to the gas stations, so

the capacity of Station 1 is kept low to increase the frequency response challenge. Reducing the thermal generator capacity also takes the generation mix closer to that found in the Nordic grid.

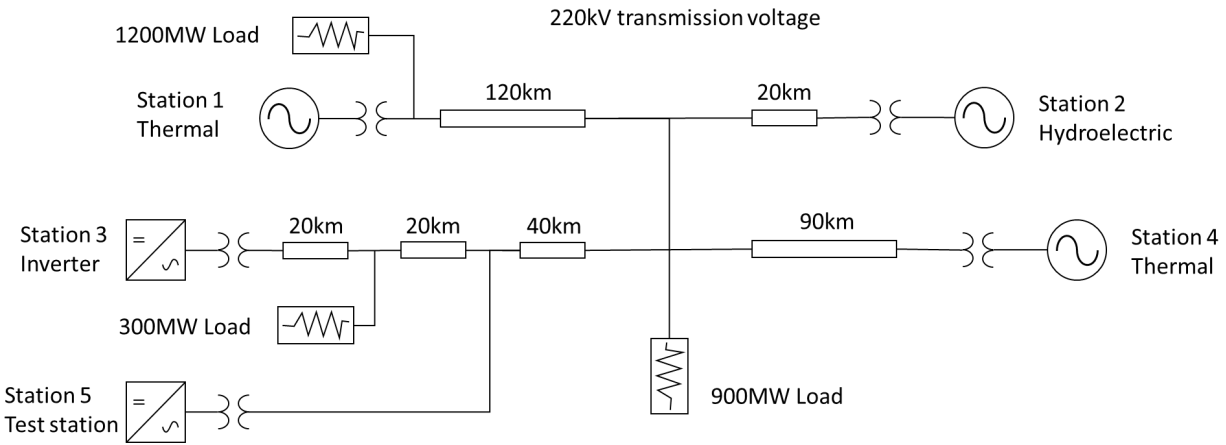


Figure 38 Grid model layout

Table 10 Test scenario parameters

Station	Type	Capacity (MVA)	Initial Power (PU)
1	Gas	500	0.27
2	Hydroelectric	1,600	0.54
3	Inverter	1,000	0.5
4	Generic thermal	500	1
5	Hydro (FSHP or VSHP)	600	0.5

The scenario was modelled using the fixed-speed system for station 5, as well as the variable-speed system using the conventional vector current controller and virtual synchronous machine. For the fixed-speed system, the permanent droop gives a 0.2 PU increase in power for a 0.5Hz frequency drop, up to the maximum capability of the plant. For the variable-speed system, the primary- and secondary-response droops are set to give a 0.3 PU increase in power for a 0.5Hz frequency drop, capped at 0.5Hz.

The response for the fixed-speed system is shown in Figure 39. The initial transient causes significant oscillations, with the gas station providing the fastest response, and the hydro station, which uses the inbuilt model, providing the slowest. Interactions of the different controllers lead to some ripple in the frequency recovery.

The response of the variable-speed system with vector current controller is shown in Figure 40. The variable-speed plant is able to provide a significant primary response, reducing the rate at which the frequency drops, although this must be reduced after 20s to limit the drop in turbine speed. Using the virtual synchronous machine controller gives the response shown in Figure 41, which is largely similar to that seen with the vector current controller. A slight reduction in the frequency and power spikes can be observed with the VSM.

A comparison of the grid frequencies for all three tests, measured from the generator speed at station 2, is shown in Figure 42, with more detail of the initial transient in Figure 43. Interestingly,

while the variable-speed systems reduce the frequency dip significantly through the instantaneous power availability, they result in a slower frequency recovery, although with lower oscillation. Comparing Figure 39 to Figure 40, it can be seen that the reduced initial frequency dip in the variable-speed systems reduces the frequency support provided by the other stations, and the frequency later starts to dip further once the primary response is exhausted. This effect would be less significant if the variable-speed system were operated at a lower initial power output, giving a greater margin.

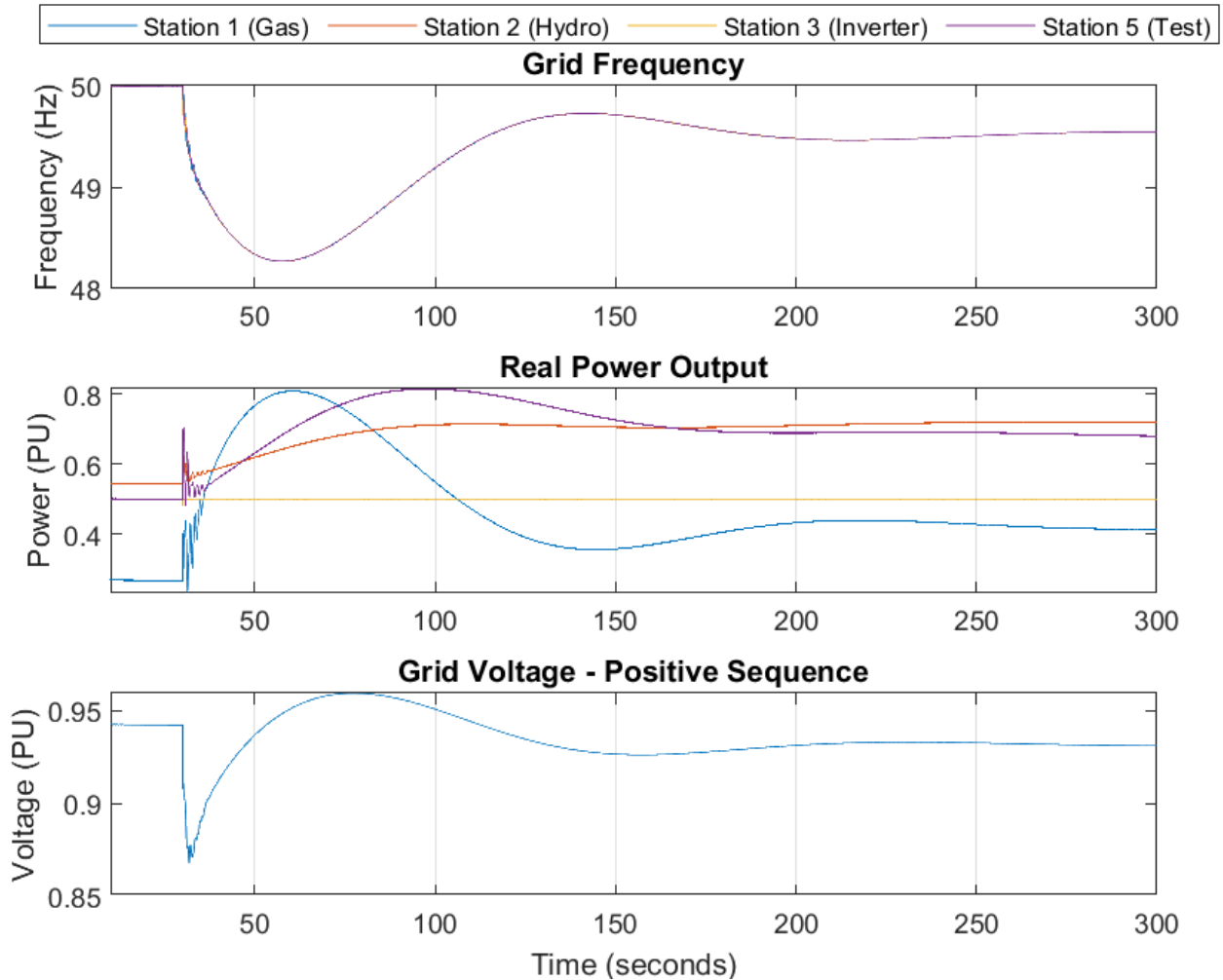


Figure 25 Grid response using fixed-speed hydro plant

The variable-speed system with VSM also results in a slightly larger frequency dip than the vector current controller. This can be explained by Figure 43, in which the emulated inertia leads to a reduction in the initial rate of change of frequency. This takes more energy from the turbine rotor, leading to a greater reduction in power during the secondary response phase, and hence a greater frequency dip later on. Both variable-speed systems result in a greatly reduced frequency oscillation, even though no explicit power system stabiliser is implemented.

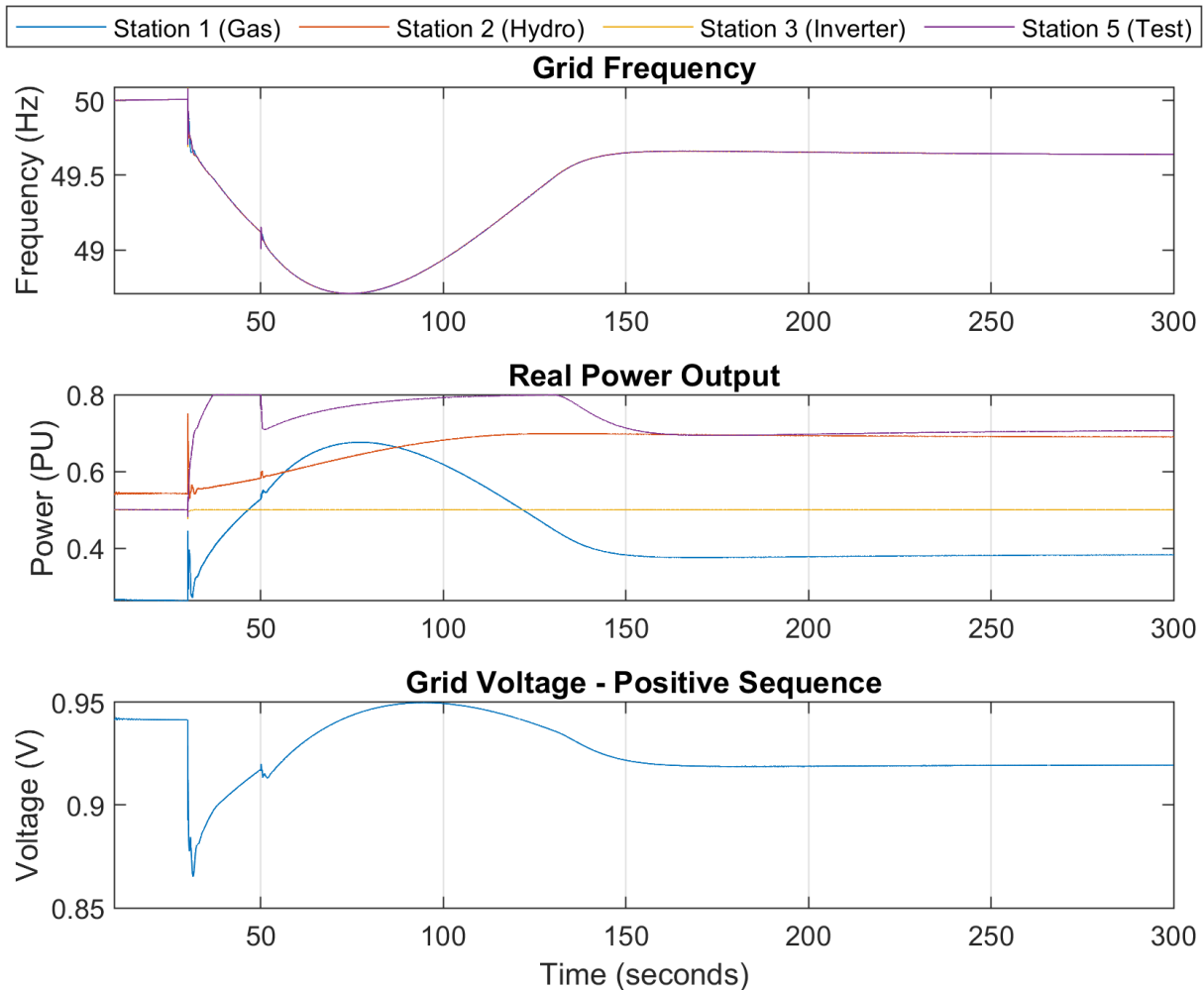


Figure 40 Grid response using variable-speed hydro plant, and vector current controller

Detail of the power transient in the first few seconds at station 2 is shown in Figure 44, in which both variable-speed systems can be seen to reduce the level of power oscillations compared with the fixed-speed system. The initial transient is highest with the vector current controller, this is due to the reduced system inertia meaning that the other stations must provide a larger share of the inertial response. The variable-speed system with virtual synchronous machine results in a similar transient to the fixed-speed system, indicating that the virtual synchronous machine is providing an accurate emulated inertia.

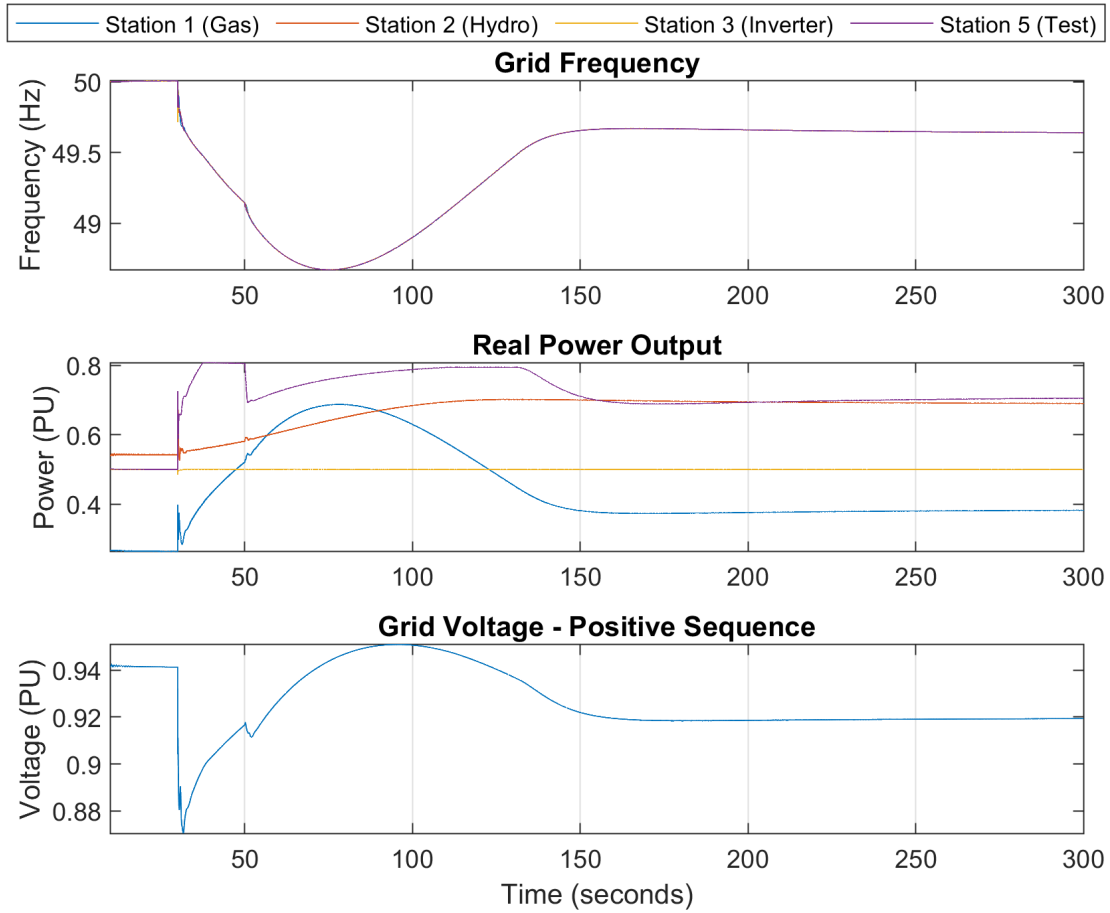


Figure 41 Grid response using variable-speed hydro plant, and virtual synchronous machine

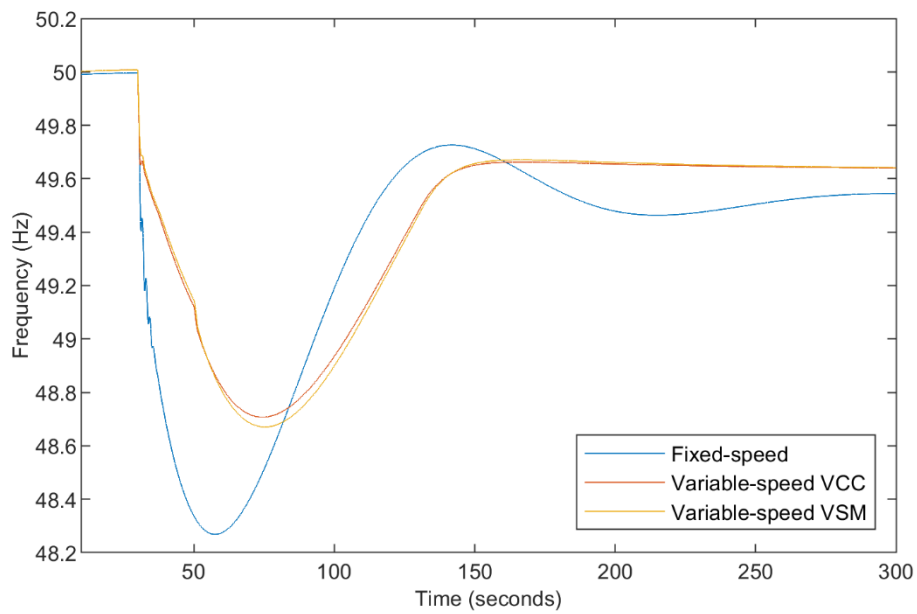


Figure 42 Comparison of grid frequencies at Station 2

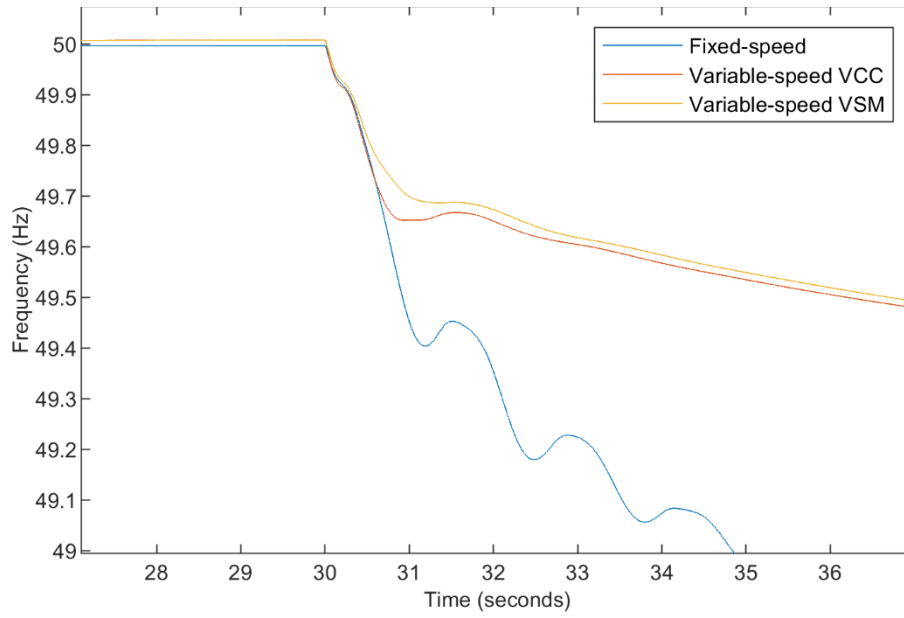


Figure 43 Detail of initial grid frequency transient at station 2

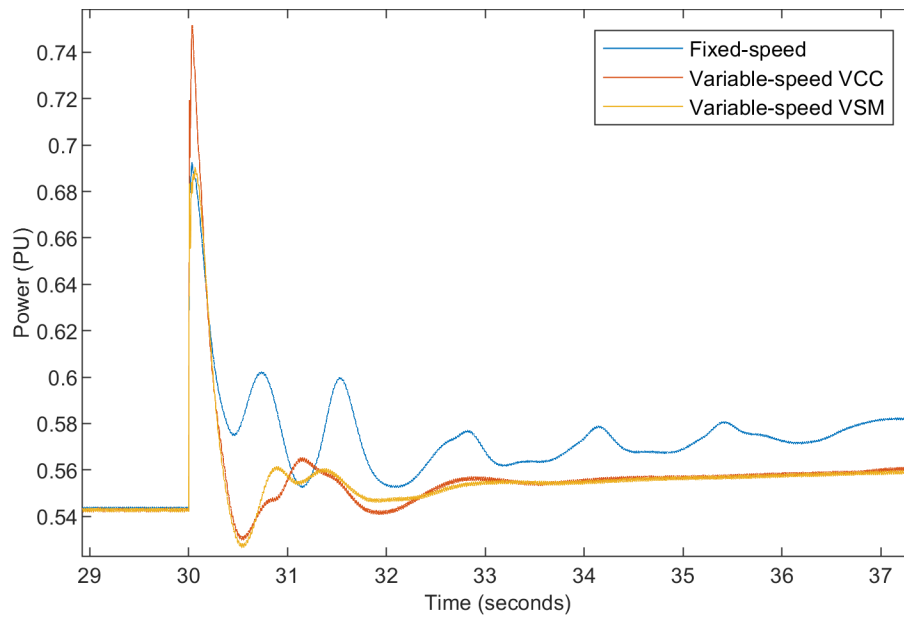


Figure 26 Detail of initial power transient at station 2

5 Conclusion

A control system has been designed for a variable-speed hydropower plant based around a synchronous generator and fully-rated power converter, making it suitable for retrofitting to an existing plant. The control system is designed primarily to provide fast frequency support services to the electrical grid, by making use of the stored energy in the turbine and generator inertia, while avoiding undesirable operating speeds for the turbine.

Operation of the frequency support controller has been verified in simulation using a stiff grid, with the plant able to provide instantaneous increases in power output in response to a drop in the grid frequency. Performance has been further verified in simulations with a representative grid, in which the energy mix has been selected to favour a larger quantity of slower-reacting hydroelectric power and a lower amount of thermal generation, in addition to a significant amount of inverter-connected generation. In this scenario, in which a frequency event is triggered by disconnecting a plant representing 20% of the total generation output, variable-speed operation of the hydroelectric power plant is found to significantly reduce the depth of the frequency dip compared with fixed-speed operation.

In addition to a conventional vector current controller for the hydropower converter, a controller based on a virtual synchronous machine has been implemented. Testing using a stiff grid has verified the ability to provide synthetic inertia, and this can be tuned for increased damping compared with a real synchronous generator. Furthermore, the virtual inertia can be increased above that of the generator used, although this will result in a greater drop in generator speed.

In simulation using the representative grid, the virtual synchronous machine operation results in a reduction in the initial rate of change of frequency, resulting in a lower frequency dip. However, the ultimate frequency dip is greater as the energy in the turbine inertia is exhausted more quickly. Thus the synthetic inertia could be useful in compensating for a reduced system inertia due to a larger proportion of inverter-connected generation, especially if the virtual inertia is increased above that of the generator. However, it is clear that synthetic inertia provision will conflict with the ability to provide frequency support services.

6 References

- Balas, G. J. (2002). Linear Parameter-Varying Control and Its Application to Aerospace Systems. *ICAS 2002 CONGRESS*. Toronto.
- Beus, M., & Pandžić, H. (2018). Application of Model Predictive Control Algorithm on a Hydro Turbine Governor Control. *20th Power Systems Computation Conference, PSCC 2018*. Dublin, Ireland.
- Briat, C. (2015). Linear Parameter Varying and Time-delay Systems: Analysis, Observation, Filtering & Control. In Silviu-Iulian, *Advances in Delays and Dynamics*. Springer-Verlag.
- Cloutier, J. (1997). State-Dependent Riccati Equation Techniques: An Overview. *American Control Conference*, (pp. 932-936).
- D'Arco, S., & Suul, J. (2013). Virtual synchronous machines - classification of implementations and analysis of equivalence to droop controllers for microgrids. *IEEE Grenoble Conference*.
- Fraile-Ardanuy, J., Román Wilhelmi, J., Fraile-Mora, J. J., & Pérez, J. I. (2006). Variable-Speed Hydro Generation: Operational Aspects and Control. *IEEE Transactions on Energy Conversion*, 21(2), 569-574.
- Harnefors, L., & Nee, H.-P. (1998). Model-Based Current Control of AC Machines Using the Internal Model Control Method. *IEEE Transactions on Industry Applications*, 34(1), 133-141.
- Henderson, C., Vozikis, D., Holliday, D., Bian, X., & Egea-Àlvarez, A. (2020). Assessment of Grid-Connected Wind Turbines with an Inertia Response by Considering Internal Dynamics. *Energies*, 30(5), 1038.
- Iliev, I., Trivedi, C., & Dahlhaug, O. (2019). Variable-speed operation of Francis turbines: A review of the perspectives and challenges. *Renewable and Sustainable Energy Reviews*, 103, 109-121.
- Krause, P., Wasynczuk, O., Sudhoff, S., & Pekarek, S. (2013). *Analysis of Electrical Machinery and Drive Systems*. Wiley.
- Kuwabara, T., Shibuya, A., Furuta, H., Kita, E., & Mitsuhashi, K. (1996). Design and dynamic response characteristics of 400MW adjustable speed pumped storage unit for ohkawachi power station. *IEEE Transactions on Energy Conversion*, 11(2), 376-384.
- Mercier, T., Olivier, M., & Dejaeger, E. (2016). Operation ranges and dynamic capabilities of variable-speed pumped-storage hydropower. *Journal of Physics: Conference Series*, 813.
- Muñoz-Hernández, G. A., & Jones, D. (2006). MIMO Generalized Predictive Control for a Hydroelectric Power Station. *IEEE Transactions on Energy Conversion*, 21(4), 921-929.
- National Grid Electricity System Operator Limited. (2020, May 7). The Grid Code. (5). UK.
- Nielsen, T. K. (2015). Simulation model for Francis and Reversible Pump Turbines. *International Journal of Fluid Machinery and Systems*, 8(3), 169-182.
- Nobile, E., Sari, G., & Schwery, A. (2018). Variable Speed Hydro Pumped Storage as Flexible Enabler of Intermittent Renewable Penetration. *IEEE Power and Energy Society General Meeting*. Portland, USA.

- Ogasawara, S., Akagi, H., & Nabae, A. (1988). The Generalized Theory of Indirect Vector Control for AC Machines. *IEEE Transactions on Industry Applications*, 24(3), 470-478.
- Pannatier, Y., Kawkabani, B., Nicolet, C., Simond, J.-J., Schwery, A., & Allenbach, P. (2010). Investigation of Control Strategies for Variable-Speed Pump-Turbine Units by Using a Simplified Model of the Converters. *IEEE Transactions on Industrial Electronics*, 57(9), 3039-3049.
- Reigstad, T. I., & Uhlen, K. (2020). Variable Speed Hydropower Conversion and Control. *IEEE Transactions on Energy Conversion*, 35(1), 386-393.
- Reigstad, T.I., & Uhlen, K. (2020). Optimized Control of Variable Speed Hydropower for Provision of Fast Frequency Reserves. *Electric Power Systems Research*.
- Reigstad, T.I., & Uhlen, K. (2021). Nonlinear Model Predictive Control of Variable Speed Hydropower for Provision of Fast Frequency Reserves. *Electric Power Systems Research*.
- Reigstad, T.I., & Uhlen, K. (2021). Variable Speed Hydropower for Provision of Fast Frequency Reserves in the Nordic Grid. *IEEE Transactions on Power Systems*, 5476-5485.
- Steimer, P. K., Senturk, O., Aubert, S., & Linder, S. (2014). Converter-fed synchronous machine for pumped storage plants. *IEEE Energy Conversion Congress and Exposition (ECCE)*. Pittsburgh, USA.
- Uzel, D., Zeman, K., Peroutka, Z., & Danek, M. (2012). Optimal Vector Control for Wound Rotor Salient Pole Synchronous Motor Up to Base Speed. *15th International Power Electronics and Motion Control Conference (EPE-PEMC)*. Novi Sad, Serbia.
- Valavi, M., & Nysveen, A. (2016). Variable-speed operation of hydropower plants: past, present, and future. *XXII International Conference on Electrical Machines (ICEM)*. Lausanne, Switzerland.
- Vargas-Serrano, A., Hamann, A., Hedtke, S., Franck, C. M., & Hug, G. (2017). Economic Benefit Analysis of Retrofitting a Fixed-Speed Pumped Storage Hydropower Plant with an Adjustable-Speed Machine. *IEEE PowerTech*. Manchester.
- Working Group on Prime Mover and Energy Supply Models for System Dynamic Performance Studies. (1992). Hydraulic Turbine and Turbine Control Models for System Dynamic Studies. *IEEE Transactions on Power Systems*, 7(1), 167-179.
- Yang, W., & Yang, J. (2019). Advantage of variable-speed pumped storage plants for mitigating wind power variations: Integrated modelling and performance assessment. *Applied Energy*, 237, 720-732.
- Zhang, L., Harnefors, L., & Nee, H.-P. (2010). Power-Synchronization Control of Grid-Connected Voltage-Source Converters. *IEEE Transactions on Power Systems*, 25(2), 809-820.
- Zhang, R., Chen, D., & Ma, X. (2015). Nonlinear Predictive Control of a Hydropower System Model. *Entropy*, 17, 6129-6149.
- Zhang, R., Chen, D., & Ma, X. (2015). Nonlinear Predictive Control of a Hydropower System Model. *Entropy*, 6129-6149.

- Zhang, R., Chen, D., Yao, W., Ba, D., & Ma, X. (2017). Non-linear fuzzy predictive control of hydroelectric system. *IET Generation, Transmission & Distribution*, 11(8), 1966-1975.
- Zheng, Y., Zhou, J., Zhu, W., Zhang, C., Li, C., & Fu, W. (2016). Design of a multi-mode intelligent model predictive control strategy for hydroelectric generating unit. *Neurocomputing*, 207, 287-299.
- Zhou, W., Thoresen, H.M., & Glemmstad, Bjorn. (2012). Application of Kalman filter based nonlinear MPC for Flood Gate control of Hydropower plant. *IEEE Power and Energy Society General Meeting*.